Journal of Non-Newtonian Fluid Mechanics 321 (2023) 105101

Contents lists available at ScienceDirect

Journal of Non-Newtonian Fluid Mechanics

journal homepage: www.elsevier.com/locate/jnnfm

Homogenizing the viscosity of shear-thinning fiber suspensions with an FFT-based computational method

Benedikt Sterr [a], Daniel Wicht [a], Andrew Hrymak [b], Matti Schneider [a], Thomas Böhlke [a,*]

[a] Karlsruhe Institute of Technology (KIT), Institute of Engineering Mechanics, Germany
[b] University of Western Ontario, Department of Chemical and Biochemical Engineering, Canada

ARTICLE INFO

Keywords:
Effective viscosity
Fiber-reinforced composites
Non-Newtonian
FFT-based method
Cross-fluid

ABSTRACT

In this work, we investigate the fiber orientation dependent viscosity of fiber suspensions using a computational homogenization method. To improve computational prediction capabilities for the viscosity of fiber suspensions, we extend an existing, Fast Fourier Transform based computational approach for fiber suspensions with linear viscous, i.e., Newtonian, matrix behavior to nonlinear viscous matrix behavior. Specifically, a Cross-type shear-thinning rheology is assumed for the matrix fluid. We employ composite voxels to lower resolution requirements and find through resolution studies that the resolution error decreases for certain shear rates. Furthermore, we conduct a volume element study and find that the representative volume element sizes for engineering considerations in a specific Newtonian case and the investigated Cross-type case are highly similar. For shear rates of engineering process interest we visualize the effective suspension viscosity in three dimensions and study the effects of the fiber volume fraction and the imposed macroscopic shear rate tensor on the suspension viscosity. We find that the elongational viscosity and the degree of anisotropy of the suspension viscosity vary stronger with the shear rate for higher fiber volume fractions. In a comparison with an analytical mean-field model for the suspension viscosity, the deviations between the computational and analytical results turn out to be substantial.

1. Introduction

1.1. State of the art

In engineering manufacturing processes of composite parts, such as injection and compression molding, the anisotropic viscosity of fiber polymer suspensions has profound influence on the manufacturing process and the material properties of the final part [1]. The effective suspension viscosity influences the appropriate choice of various process parameters, such as screw speed and back pressure in injection molding [2], as well as press force and mold temperature in compression molding [3]. In addition, the flow field, and thus the final material properties of the finished part also depend on the suspension viscosity [4].

Even though the suspension viscosity is a quantity of direct engineering interest, it is difficult to determine the full viscosity tensor by experimental methods. This is partly because it is challenging to ensure a specific fiber orientation state during rheology experiments [5], and the suspension viscosity depends strongly on the fiber orientation [6]. Furthermore, fibers break during rheometer studies, which also affects the suspension viscosity [5]. Last but not least, the dependence of the suspension viscosity on shear rate and temperature [7] further complicates matters. As a result, tensorial and scalar analytical homogenization methods are commonly used in conjunction with scalar experiments to understand and predict the local suspension viscosity.

Since Sutherland's [8] and Einstein's [9] work on the effective scalar viscosity of dilute suspensions of spherical particles in Newtonian fluids, a variety of analytical approaches to model the complete tensorial viscosity of suspensions were suggested. For dilute and semidilute suspensions of slender rods in Newtonian fluids, models were proposed among others by Batchelor [10,11], Dinh and Armstrong [12], as well as Shaqfeh and Frederickson [13]. For an overview of anisotropic mean-field homogenization models of particle suspensions in Newtonian fluids we refer the reader to Karl and Böhlke [14]. Various other models are detailed in Petrie [15].

In the case of suspensions with non-Newtonian matrix behavior, multiple models [16–19] were developed based on second order fluid theory. However, these models are restricted to a single suspended particle. Brunn [19] also applied his single particle model to dilute suspensions and found that the model could not capture hydrodynamic particle–particle interactions. In a shear-thinning power law setting,

* Corresponding author.
E-mail address: thomas.boehlke@kit.edu (T. Böhlke).

https://doi.org/10.1016/j.jnnfm.2023.105101
Received 1 March 2023; Received in revised form 30 June 2023; Accepted 21 July 2023
Available online 28 July 2023

Goddard [20,21] developed a model for dilute suspensions, which was found to be qualitatively promising but quantitatively inaccurate by himself [22] and Mobuchon et al. [23]. Later, Pipes et al. [24, 25] proposed a model for the concentrated and hyperconcentrated regime in a power law setting. Even though the results agree well with experimental data by Binding [5], the model is limited by its assumption of unidirectional and fixed fiber arrays. The prediction accuracy of another power-law model by Souloumiac and Vincent [26] varies strongly with the shear rate and fiber volume fraction, making it difficult to apply appropriately. Also, more recent models [27–30] have yet to be established as valid over a wide range of temperatures, shear rates, fiber-orientation states and fiber aspect ratios. Overall, holistic theoretical treatment of all physical effects in fiber suspensions proves to be a difficult task.

As a result, computational methods offer unique insights into the physics of fiber suspensions. As fiber suspension problems often involve Stokes flow, computational techniques focused on problems in the Stokes flow regime are of particular interest. Marin et al. [31] introduced a highly accurate Boundary Element Method (BEM) to treat confined Stokes flow and successfully applied it to a problem with a single sphere suspended in a Newtonian fluid. Subsequently, the BEM based approach used by Marin et al. [31] could also be extended to different geometries and multiple suspended bodies. To treat complex particle geometries suspended in Newtonian fluids, Balboa et al. [32] employed a method where particles are modeled via a rigid collection of connected spheres called "multiblob". Balboa et al. [32] successfully applied their multiblob approach to Stokes flow problems near walls and in channels, involving multiblobs of different geometries such as spheres and cylinders. Furthermore, Fast Fourier Transform (FFT) based computational techniques, that were first popularized in solid mechanics [33,34], were also successfully applied to Stokes flow problems involving Newtonian fluids. In combination with the RVE method [35], the FFT-based computational approach was used to solve problems in porous media [36–38], and to compute the effective viscosity of fiber suspensions with Newtonian matrix behavior [39]. More details regarding FFT-based techniques can be found in recent review articles [40–42].

Computational methods were also employed to treat suspensions with non-Newtonian matrix fluids. Domurath et al. [43] used the Finite Element Method (FEM) to study the effective viscosity of a dilute suspension with a single spherical particle suspended in a Bird-Carreau fluid. For non-dilute suspensions, Traxl et al. [44] used a FEM-based approach to investigate the effective viscosity of suspensions with noncolloidal angular, as well as spherical pores and particles in generalized-Newtonian fluids. The investigations of Traxl et al. [44] consider suspensions with spherical, hexahedral, and tetrahedral particles, as well as matrix fluids with Newtonian, Power-law, Cross-type, and von Mises-type behavior. Švec et al. [45] studied rheological properties of suspensions with rigid spherical particles and fibers suspended in Newtonian and non-Newtonian matrix fluids. To do so, Švec et al. [45] used a computational framework combining the lattice Boltzmann method for fluid flow, a mass tracking algorithm for free surface representation, and an immersed boundary approach to consider interactions between the fluid and the particles.

1.2. Contributions

In this article, with regard to the difficult experimental and theoretical treatment of fiber suspensions with non-Newtonian matrix behavior, we apply FFT-based computational methods to study the viscosity of such suspensions. Using FFT-based computational methods allows us to leverage highly efficient implementations of the Fast Fourier Transform, powerful non-linear equation solvers, and discretizations with regular grids. This enables the study of fiber suspensions with microstructures that are otherwise difficult to discretize and investigate using interface-conforming mesh based approaches. Thus, we extend the approach for suspensions with Newtonian matrix behavior detailed by Bertóti et al. [39] to suspensions with non-Newtonian, Cross-type [46,47] shear-thinning fluids. In Section 2, we approach the effective suspension viscosity from a theoretical and a computational perspective, and make use of an interpolation based matrix equation to estimate the anisotropic, non-Newtonian suspension viscosity from a limited number of computational experiments. As the physical basis for our investigations, we use a Cross-type material law to model the viscosity behavior of a commercially available PA6, and study suspension microstructures with fibers of aspect ratio ten. In preliminary investigations to identify the resolution of the discretized suspension microstructure, we find that the resolution error of the effective stresses can depend favorably on the shear rate, see Section 3.2. Through a volume element size study, we find that the necessary volume element size for engineering considerations are highly similar in a specific Newtonian case and the investigated non-Newtonian case, see Section 3.3. As our main contribution, we visualize and discuss in Section 4 how the shear rate and fiber volume fraction influence the magnitude and degree of anisotropy of the suspension viscosity. We observe that the viscosity magnitude decreases with the shear rate until a Cross-type model intrinsic, minimum viscosity is reached. In contrast, the degree of anisotropy depends on the degree to which the matrix behaves nonlinearly. Additionally, we find that the dependence of both the magnitude and the degree of anisotropy on the shear rate is increased for higher fiber volume fractions. In a comparison between an analytical mean-field model and our computational results, we observe large discrepancies in the predicted viscosities.

2. Computing the effective viscosity of particles suspended in a nonlinear viscous medium

2.1. The nonlinear viscosity tensor

For an incompressible Newtonian fluid, the strain rate tensor $\boldsymbol{D} \in \mathrm{Sym}_0$ and the non-equilibrium viscous stress tensor $\boldsymbol{\tau} \in \mathrm{Sym}_0$ are related by the constitutive law

$$\boldsymbol{\tau} = 2\eta\, \boldsymbol{D}, \tag{2.1}$$

involving a shear viscosity η. Here, $\mathrm{Sym}_0(3)$ denotes the vector space of symmetric and traceless second-order tensors. More generally, non-Newtonian models [7] may be considered where the viscosity depends on the scalar shear rate $\dot{\gamma} = \sqrt{2}\,\|\boldsymbol{D}\|$ with the norm $\|\boldsymbol{D}\| = \sqrt{\boldsymbol{D} \cdot \boldsymbol{D}}$.

Cross-type [46,47] material models are able to predict the shear-thinning rheology of polymers accurately [7]. Their viscosity is governed by an expression of the form

$$\eta(\dot{\gamma}) = \eta_\infty + \frac{\eta_0 - \eta_\infty}{1 + (k\dot{\gamma})^m}, \tag{2.2}$$

with positive material parameters $\eta_0 \geq \eta_\infty$, k, and m.

For the shear rate limits $\dot{\gamma} \to 0$ and $\dot{\gamma} \to \infty$, the scalar viscosity $\eta(\dot{\gamma})$ approaches the initial viscosity η_0 and the asymptotic viscosity η_∞, respectively. The two material parameters k and m control the transition region between the viscosities η_0 and η_∞.

To describe suspensions of non-spherical particles, it is convenient to consider more general, anisotropic viscosity tensors $\mathbb{V} \in L(\mathrm{Sym}_0(3))$ and constitutive relations of the form [48,49]

$$\boldsymbol{\tau} = \mathbb{V}[\boldsymbol{D}], \tag{2.3}$$

where L refers to the linear transformations on a given vector space, and the viscosity tensor $\mathbb{V}$ depends on the fiber arrangement and the fiber orientation distribution. If the suspending fluid is itself non-Newtonian, the suspension will, in general, be governed by a constitutive relation of the form

$$\boldsymbol{\tau} = \mathbb{V}(\boldsymbol{D})[\boldsymbol{D}] \tag{2.4}$$

with a viscosity tensor $\mathbb{V}$ that additionally depends on the shear-rate tensor $\boldsymbol{D}$. By the dissipation inequality, the viscosity tensor $\mathbb{V}(\boldsymbol{D})$ must

be positive semidefinite for all shear rates $\boldsymbol{D}$, while the major symmetry of the viscosity tensor $\mathbb{V}(\boldsymbol{D})$ is required in the linear case for Onsager's relations to be satisfied [50]. Existence of a dissipation potential is sufficient for the major symmetry of the viscosity tensor $\mathbb{V}(\boldsymbol{D})$ in the nonlinear case, see Šilhavý [50, Sec. 12.3.1]. For the general formulation of a dissipation potential with temperature and mass density dependence, also see Šilhavý [50, Sec. 12.3.1].

For the subsequent derivations, we will look at a special case that is sufficient for our purposes. Assume that for constant temperature and density a twice continuously differentiable dissipation potential $\Psi : \mathsf{Sym}_0(3) \to \mathbb{R}$ is given, which furthermore satisfies the condition

$$\frac{\partial \Psi}{\partial \boldsymbol{D}}(\boldsymbol{0}) = \boldsymbol{0}. \tag{2.5}$$

Then, the non-equilibrium viscous stress $\boldsymbol{\tau}$ is governed by the relationship

$$\boldsymbol{\tau} = \frac{\partial \Psi}{\partial \boldsymbol{D}}(\boldsymbol{D}), \tag{2.6}$$

and by the fundamental theorem of calculus, we may write

$$\frac{\partial \Psi}{\partial \boldsymbol{D}}(\boldsymbol{D}) = \int_0^1 \frac{\mathrm{d}}{\mathrm{d}s}\left[\frac{\partial \Psi}{\partial \boldsymbol{D}}(s\boldsymbol{D})\right]\mathrm{d}s = \int_0^1 \frac{\partial^2 \Psi}{\partial \boldsymbol{D}^2}(s\boldsymbol{D})\mathrm{d}s\,[\boldsymbol{D}] \equiv \mathbb{V}(\boldsymbol{D})[\boldsymbol{D}]. \tag{2.7}$$

Thus, the viscosity tensor

$$\mathbb{V}(\boldsymbol{D}) \equiv \int_0^1 \frac{\partial^2 \Psi}{\partial \boldsymbol{D}^2}(s\boldsymbol{D})\mathrm{d}s \tag{2.8}$$

has major symmetries, as a consequence of Schwarz' theorem on the commutativity of the second partial derivatives of a twice continuously differentiable function. Thus, for any given dissipation potential, the associated viscosity tensor (2.8) automatically has the major symmetry.

It is not difficult to construct dissipation potentials both for the Newtonian (2.1) and the Cross model (2.2), i.e.,

$$\Psi(\boldsymbol{D}) = \left(\eta_\infty + (\eta_0 - \eta_\infty)\,{}_2F_1\left(1, \frac{2}{m}, \frac{2+m}{m}, -(k\dot\gamma)^m\right)\right)\frac{\dot\gamma^2}{2} \tag{2.9}$$

involving the hypergeometric function ${}_2F_1$. In the Newtonian case, it holds that $\eta = \eta_0 = \eta_\infty$, and thus

$$\Psi(\boldsymbol{D}) = \eta\, \boldsymbol{D} \cdot \boldsymbol{D} \tag{2.10}$$

The advantage of using the representation by a dissipation potential is that this potential form is preserved under a change of scales, i.e., by homogenization [51,52]. Subsequently, the viscosity tensor is accessible via a postprocessing step, see Eq. (2.8).

Actually, due to the presence of infinitely viscous inclusions, it is more convenient to work with the complementary potential Φ which arises as the Legendre–Fenchel dual

$$\Phi(\boldsymbol{\tau}) := \sup\left\{\boldsymbol{\tau} \cdot \boldsymbol{D} - \Psi(\boldsymbol{D}) \,|\, \boldsymbol{D} \in \mathsf{Sym}_0(3)\right\} \tag{2.11}$$

of the dissipation potential Ψ. The potential Ψ must grow superlinearly and be non-negative for Φ to be a proper function, i.e., not infinite everywhere. Then, as a consequence of the Fenchel–Moreau identity [53, Eq. (3.8)], the constitutive law (2.6) may be written in dual form

$$\boldsymbol{D} = \frac{\partial \Phi}{\partial \boldsymbol{\tau}}(\boldsymbol{\tau}). \tag{2.12}$$

From this, similar to the viscosity $\mathbb{V}$, the fluidity tensor $\mathbb{F}$ follows as

$$\mathbb{F}(\boldsymbol{\tau}) \equiv \int_0^1 \frac{\partial^2 \Phi}{\partial \boldsymbol{\tau}^2}(s\boldsymbol{\tau})\mathrm{d}s. \tag{2.13}$$

In the Newtonian case, the viscosity $\mathbb{V}$ and the fluidity $\mathbb{F}$ constitute the kinetic coefficients [50]. In addition to the presented context, the aforementioned potential framework can also be applied in the context of the rigid-viscoplastic modeling of polycrystals. See, e.g., Böhlke and Bertram [54] and Böhlke [55], where the viscoplastic behavior of single crystals and polycrystals is modeled via a nonlinear viscous approach.

2.2. Scale transition in nonlinear viscosity

Locally, the balance of linear momentum

$$\operatorname{div} \boldsymbol{\tau} - \nabla p = \boldsymbol{0} \tag{2.14}$$

results from a split of the stress $\boldsymbol{\sigma}$ inside the material into an unknown, periodic pressure field $p : Y \to \mathbb{R}$ and the local viscous stress field

$$\boldsymbol{\tau} = \mathcal{T}(\cdot, \bar{\boldsymbol{D}} + \nabla^{\mathrm{s}}\boldsymbol{v}), \tag{2.15}$$

and needs to be satisfied. Here, the pressure p acts as a reaction stress due to incompressibility. We consider a rectangular volume $Y \subseteq \mathbb{R}^3$, and suppose that a heterogeneous dissipation potential density $\Psi : Y \times \mathsf{Sym}_0(3) \to \mathbb{R}$ is given which satisfies the conditions discussed in the previous section pointwise. The associated stress operator reads

$$\mathcal{T} : Y \times \mathsf{Sym}_0(3) \to \mathsf{Sym}_0(3), \tag{2.16}$$

$$(\boldsymbol{x}, \boldsymbol{D}) \mapsto \frac{\partial \Psi}{\partial \boldsymbol{D}}(\boldsymbol{x}, \boldsymbol{D}). \tag{2.17}$$

The effective dissipation potential is defined as

$$\bar\Psi(\bar{\boldsymbol{D}}) = \inf\left\langle \Psi(\cdot, \bar{\boldsymbol{D}} + \nabla^{\mathrm{s}}\boldsymbol{v})\right\rangle_Y \quad \text{for} \quad \bar{\boldsymbol{D}} \in \mathsf{Sym}_0(3), \tag{2.18}$$

where the infimum is taken over all periodic velocity fields $\boldsymbol{v} : Y \to \mathbb{R}^3$ with vanishing divergence and the operator $\langle\cdot\rangle_Y$ denotes the spatial average

$$\langle\cdot\rangle_Y \equiv \frac{1}{|Y|}\int_Y (\cdot)\mathrm{d}\boldsymbol{x} \quad \text{with} \quad |Y| \equiv \int_Y \mathrm{d}\boldsymbol{x}. \tag{2.19}$$

The effective shear stress $\bar{\boldsymbol{\tau}} \in \mathsf{Sym}_0(3)$ then arises from the relationship

$$\bar{\boldsymbol{\tau}}(\bar{\boldsymbol{D}}) = \frac{\partial \bar\Psi}{\partial \bar{\boldsymbol{D}}}(\bar{\boldsymbol{D}}), \tag{2.20}$$

which is similar to Eq. (2.6). Equivalently, the effective stress may be computed by averaging the local shear stress

$$\bar{\boldsymbol{\tau}}(\bar{\boldsymbol{D}}) = \left\langle \mathcal{T}(\cdot, \bar{\boldsymbol{D}} + \nabla^{\mathrm{s}}\boldsymbol{v})\right\rangle_Y, \tag{2.21}$$

where the periodic velocity field $\boldsymbol{v}$ solves the Euler–Lagrange equation of the variational problem (2.18)

$$\operatorname{div} \boldsymbol{\tau} - \nabla p = \boldsymbol{0}, \tag{2.22}$$

which equals the balance of linear momentum (2.14). The described procedure permits to compute the effective viscosity of a mixture of viscous materials. However, we are interested in the effective viscosity of a suspension, i.e., of a mixture involving rigid inclusions. Because the viscosity inside these inclusions is infinite, the differential Eq. (2.14) is not well defined. To handle this issue, we transfer to a dual formulation. Inside the infinitely viscous inclusions, the fluidity, i.e., the inverse of the viscosity, vanishes identically. Consequently, the associated equations are well defined.

Instead of the effective dissipation potential (2.18) one may consider the effective complementary potential $\bar\Phi$, a function of the effective shear stress $\bar{\boldsymbol{\tau}}$, from which the constitutive law

$$\bar{\boldsymbol{D}}(\bar{\boldsymbol{\tau}}) = \frac{\partial \bar\Phi}{\partial \bar{\boldsymbol{\tau}}}(\bar{\boldsymbol{\tau}}), \tag{2.23}$$

arises dual to the primal relationship (2.20). To obtain the effective viscosity, a strategy based on the effective complementary potential requires to invert the effective law (2.23). To avoid this difficulty, we use mixed "boundary conditions" [56], i.e., we consider the dual variational principle, but prescribe the effective shear rate tensor $\bar{\boldsymbol{D}}$. The convex dual of the variational problem (2.18) reads

$$\left\langle \Phi(\cdot, \boldsymbol{\tau}) - \boldsymbol{\tau} \cdot \bar{\boldsymbol{D}}\right\rangle_Y \longrightarrow \inf, \tag{2.24}$$

where the infimum is taken over all stress fields $\boldsymbol{\tau} : Y \to \mathsf{Sym}_0(3)$ which satisfy the equilibrium Eq. (2.14) for a suitable pressure field, see Wicht et al. [57, §4 and Appendix B].

2.3. Computational aspects and setup

After discussing theoretical aspects in the previous section, this section is dedicated to selected computational aspects concerning the fiber suspension microstructure and FFT-based procedure, starting with a solution scheme for the convex dual variational problem (2.24). The Euler–Lagrange equation of the convex dual variational problem (2.24) reads

$$\mathbb{P}_{\mathcal{E}}\left[\frac{\partial \boldsymbol{\Phi}}{\partial \boldsymbol{\tau}}(\boldsymbol{\tau}_k) - \bar{\boldsymbol{D}}\right] = \boldsymbol{0}, \tag{2.25}$$

where $\mathbb{P}_{\mathcal{E}}$ denotes the L^2-projector onto the shear stresses satisfying the equilibrium Eq. (2.14). In terms of an arbitrary stepsize α, minimizers of the Euler–Lagrange equation (2.25) are fixed points of the gradient descent scheme

$$\boldsymbol{\tau}_{k+1} = \boldsymbol{\tau}_k - \alpha\, \mathbb{P}_{\mathcal{E}}\left[\frac{\partial \boldsymbol{\Phi}}{\partial \boldsymbol{\tau}}(\boldsymbol{\tau}_k) - \bar{\boldsymbol{D}}\right], \tag{2.26}$$

which has a unique fixed point, provided the optimization problem (2.24) is convex. For a closed form expression of the action of $\mathbb{P}_{\mathcal{E}}$ in Fourier space, and an analogous derivation of a fixed point scheme in the linear case, we refer to Bertóti et al. [39, §2]. Numerical schemes based on the gradient descent iteration (2.26) require computing a strain rate $\boldsymbol{D}$ resulting from a shear stress $\boldsymbol{\tau}$ at every continuum point $\boldsymbol{x}$ and for every iteration. Treating fibers is particularly simple: the strain rate $\boldsymbol{D}$ vanishes since the inclusions are rigid.

To solve the equation

$$\boldsymbol{\tau} = 2\eta(\dot{\gamma})\, \boldsymbol{D} \tag{2.27}$$

for the strain rate $\boldsymbol{D}$, compare Eq. (2.1), we first take norms on both sides to arrive at the equation

$$\|\boldsymbol{\tau}\| = 2\eta(\dot{\gamma})\, \|\boldsymbol{D}\| \equiv \sqrt{2}\eta(\dot{\gamma})\dot{\gamma}. \tag{2.28}$$

We use Newton's method to find a root of the function

$$g(\dot{\gamma}) = \|\boldsymbol{\tau}\| - \sqrt{2}\eta(\dot{\gamma})\dot{\gamma}, \tag{2.29}$$

and thus compute iteratively

$$\dot{\gamma}_{n+1} = \dot{\gamma}_n - s_n \frac{g(\dot{\gamma}_n)}{g'(\dot{\gamma}_n)}. \tag{2.30}$$

Using backtracking for the step size s_n to ensure that the Armijo–Goldstein inequality [58,59] holds. For the Cross fluid (2.2), the derivative of the function g computes as

$$g'(\dot{\gamma}) = -\sqrt{2}\left(\eta(\dot{\gamma}) - \frac{m(\eta_0 - \eta_\infty)(k\dot{\gamma})^m}{(1 + (k\dot{\gamma})^m)^2}\right). \tag{2.31}$$

Once the scalar shear rate $\dot{\gamma}$ is identified, we compute the strain rate tensor $\boldsymbol{D}$ via

$$\boldsymbol{D} = \frac{\boldsymbol{\tau}}{2\eta(\dot{\gamma})}. \tag{2.32}$$

The fiber suspension microstructures were generated with the sequential addition and migration method [60], and discretized on a staggered grid [61] to ensure stability for incompressible material models. The resulting equation system was solved with the Barzilai–Borwein method [39,62] in the Newtonian case, while a nonlinear Newton-CG approach [63,64] was used in the Cross-type case. For validation purposes, we compared computational results of the presented FFT-based approach with computational results from literature [44], see Section 3.1. For a detailed overview on solvers for the nonlinear Lippmann–Schwinger equation in the closely related case of solid mechanics (2.26), see Schneider [65]. For proofs on the existence and uniqueness of solutions to the considered nonlinear homogenization problem (2.24), we refer to Schneider [66]. Further details on the employed FFT-based homogenization approach including solvers and discretization, we refer to Bertóti et al. [39] and Schneider [64].

To numerically obtain an effective viscosity or fluidity with the integral Eqs. (2.8) and (2.13), the respective integral, and the derivatives occurring in the integrand need to be discretized. In combination with the costly computation of the effective stresses or strains this renders the required computational effort to obtain an effective viscosity prohibitively large. Instead, we employ equation (2.7) to estimate an effective, viscosity-like quantity solely from computationally obtained effective stresses $\bar{\boldsymbol{\tau}}$, by using the following equation in Mandel's notation [39]

$$\underline{\underline{\bar{\tau}}} = \underline{\underline{\bar{V}}}\, \underline{\underline{\bar{D}}}, \quad \text{i.e.,} \quad \underline{\underline{\bar{V}}} = \underline{\underline{\bar{\tau}}}\, \underline{\underline{\bar{D}}}^{\dagger}. \tag{2.33}$$

Here, $(\cdot)^{\dagger}$ denotes the Moore–Penrose pseudoinverse which is equal to an inversion on $\mathrm{Sym}_0(3)$, $\underline{\underline{\bar{\tau}}}$ collects the computed effective stresses

$$\underline{\underline{\bar{\tau}}} = \begin{bmatrix} \bar{\tau}_{11}^{(1)} & \bar{\tau}_{11}^{(2)} & \bar{\tau}_{11}^{(3)} & \bar{\tau}_{11}^{(4)} & \bar{\tau}_{11}^{(5)} & \bar{\tau}_{11}^{(6)} \\ \bar{\tau}_{22}^{(1)} & \bar{\tau}_{22}^{(2)} & \bar{\tau}_{22}^{(3)} & \bar{\tau}_{22}^{(4)} & \bar{\tau}_{22}^{(5)} & \bar{\tau}_{22}^{(6)} \\ \bar{\tau}_{33}^{(1)} & \bar{\tau}_{33}^{(2)} & \bar{\tau}_{33}^{(3)} & \bar{\tau}_{33}^{(4)} & \bar{\tau}_{33}^{(5)} & \bar{\tau}_{33}^{(6)} \\ \sqrt{2}\bar{\tau}_{23}^{(1)} & \sqrt{2}\bar{\tau}_{23}^{(2)} & \sqrt{2}\bar{\tau}_{23}^{(3)} & \sqrt{2}\bar{\tau}_{23}^{(4)} & \sqrt{2}\bar{\tau}_{23}^{(5)} & \sqrt{2}\bar{\tau}_{23}^{(6)} \\ \sqrt{2}\bar{\tau}_{13}^{(1)} & \sqrt{2}\bar{\tau}_{13}^{(2)} & \sqrt{2}\bar{\tau}_{13}^{(3)} & \sqrt{2}\bar{\tau}_{13}^{(4)} & \sqrt{2}\bar{\tau}_{13}^{(5)} & \sqrt{2}\bar{\tau}_{13}^{(6)} \\ \sqrt{2}\bar{\tau}_{12}^{(1)} & \sqrt{2}\bar{\tau}_{12}^{(2)} & \sqrt{2}\bar{\tau}_{12}^{(3)} & \sqrt{2}\bar{\tau}_{12}^{(4)} & \sqrt{2}\bar{\tau}_{12}^{(5)} & \sqrt{2}\bar{\tau}_{12}^{(6)} \end{bmatrix} \tag{2.34}$$

and $\underline{\underline{\bar{D}}}$ collects the investigated load cases

$$\underline{\underline{\bar{D}}} = \dot{\gamma}\sqrt{\frac{2}{3}} \begin{bmatrix} 1 & -\frac{1}{2} & -\frac{1}{2} & 0 & 0 & 0 \\ -\frac{1}{2} & 1 & -\frac{1}{2} & 0 & 0 & 0 \\ -\frac{1}{2} & -\frac{1}{2} & 1 & 0 & 0 & 0 \\ 0 & 0 & 0 & \sqrt{\frac{3}{2}} & 0 & 0 \\ 0 & 0 & 0 & 0 & \sqrt{\frac{3}{2}} & 0 \\ 0 & 0 & 0 & 0 & 0 & \sqrt{\frac{3}{2}} \end{bmatrix}. \tag{2.35}$$

The ith column in the matrix $\underline{\underline{\bar{\tau}}}$ contains the effective shear stress corresponding to the particular applied shear rate that is listed in the ith column of the matrix $\underline{\underline{\bar{D}}}$. In the Newtonian case, the matrix $\underline{\underline{\bar{V}}}$ encodes the components of the viscosity tensor because of superposition. Since superposition is not generally valid in the non-Newtonian case, the matrix $\underline{\underline{\bar{V}}}$ acts as an interpolation between the six calculated effective stresses $\underline{\underline{\bar{\tau}}}$. Additionally, the load cases $\underline{\underline{\bar{D}}}$ are not uniquely defined and interpolation between the effective stresses $\underline{\underline{\bar{\tau}}}$ is qualitative in nature. However, the matrix $\underline{\underline{\bar{V}}}$ provides quantitatively robust information in the load cases collected in $\underline{\underline{\bar{D}}}$, and its interpolating property allows us to draw intuition for the results in between. Thus, even in the non-Newtonian case, the matrix $\underline{\underline{\bar{V}}}$ may be used to investigate the viscous suspension behavior. We will refer to $\underline{\underline{\bar{V}}}$ as the suspension viscosity throughout the article.

2.4. A model for the fiber suspension viscosity

To model the fiber suspension viscosity with analytical means, a few preliminary considerations regarding fiber orientation statistics are in order. We consider fiber suspensions with fiber volume fraction c_{F}, where all fibers are of the same length ℓ, and diameter d. To describe the orientation state of such a suspension, we use a fiber orientation distribution function [1]

$$\rho : S^2 \to \mathbb{R}, \quad \boldsymbol{n} \mapsto \rho(\boldsymbol{n}). \tag{2.36}$$

Per definition, the function is non-negative, integrates to unity, and is symmetric with respect to the origin such that $\rho(\boldsymbol{n}) = \rho(-\boldsymbol{n})$. Typically, it is not feasible to take the large amount of information contained in the fiber orientation distribution function into account at every spatial element of component-scale simulations. To reduce the necessary computational effort in treating fiber orientation states, it is common to use the fiber orientation tensors of second and fourth order [67,68]

$$\boldsymbol{N} = \int_{S^2} \boldsymbol{n} \otimes \boldsymbol{n}\, \rho(\boldsymbol{n})\, \mathrm{d}S(\boldsymbol{n}), \tag{2.37}$$

$$\mathbb{N} = \int_{S^2} \boldsymbol{n} \otimes \boldsymbol{n} \otimes \boldsymbol{n} \otimes \boldsymbol{n}\, \rho(\boldsymbol{n})\, \mathrm{d}S(\boldsymbol{n}). \tag{2.38}$$

Both tensors $\boldsymbol{N}$ and $\mathbb{N}$ are completely symmetric, positive semidefinite, and contract with the second-order unity tensor $\mathbf{1}$ such that

$$\boldsymbol{N} \cdot \mathbf{1} = 1, \tag{2.39}$$

$$\mathbb{N}[\mathbf{1}] = \boldsymbol{N}. \tag{2.40}$$

With these two descriptors at hand, a large variety of anisotropic mean-field models has been built to model material behavior [14]. In the case of a transversely isotropic fluid with constant viscosity, a convenient approximation of the popular Mori–Tanaka model is available with [69]

$$\begin{aligned} \mathbb{V}_{\mathsf{MT}} &= 2\eta_{\mathsf{MF}} \left(\mathbb{P}_2 + N_{\mathsf{p}}^{\mathsf{MF}}\, \mathbb{P}_2\, \mathbb{N}\, \mathbb{P}_2 \right), \\ \eta_{\mathsf{MF}} &= \frac{1 + c_{\mathsf{F}}}{1 - c_{\mathsf{F}}} \eta, \\ N_{\mathsf{p}}^{\mathsf{MF}} &= \frac{c_{\mathsf{F}}}{1 + c_{\mathsf{F}}} \frac{r_{\mathsf{a}}^2}{2(\ln(2r_{\mathsf{a}}) - 3/2)}. \end{aligned} \tag{2.41}$$

Here, η_{MF} is the effective scalar viscosity, and $N_{\mathsf{p}}^{\mathsf{MF}}$ is the particle number. This model is derived by decomposing the microstructure into m transversely isotropic pseudo domains containing a single fiber and the matrix material. In a first step, the unidirectional effective viscosities $\mathbb{V}_{\mathsf{UD}}^m$ of these m pseudodomains are approximated with the Mori–Tanaka method by

$$\mathbb{V}_{\mathsf{UD}}^m = 2\eta\, \mathbb{P}_2 + \frac{c_{\mathsf{F}}}{1 - c_{\mathsf{F}}} \mathbb{P}_m^{-1}, \tag{2.42}$$

where $\mathbb{P}_m$ is the polarization tensor depending on the matrix material properties and the fiber geometry. The expression (2.42) equals the lower Hashin–Shtrikman bound [70]. In a second step, the effective viscosity of the volume element is calculated by orientation averaging the unidirectional effective viscosities $\mathbb{V}_{\mathsf{UD}}^m$ via

$$\mathbb{V}_{\mathsf{MT}} = \frac{1}{M} \sum_{m=1}^{M} \mathbb{V}_{\mathsf{UD}}^m. \tag{2.43}$$

The Voigt-type average (2.43) yields an upper bound on the dissipation [71]. However, this model is only applicable for fluids with constant viscosity, since it does not depend on the shear rate $\dot{\gamma}$. One possible extension to incorporate shear rate dependency in the case of rigid fibers is [14]

$$\eta_{\mathsf{MF}} = \frac{1 + c_{\mathsf{F}}}{1 - c_{\mathsf{F}}} \eta \left(\frac{\dot{\gamma}}{1 - c_{\mathsf{F}}} \right), \tag{2.44}$$

which recovers the Newtonian case for the shear rate limits $\dot{\gamma} \to 0$ and $\dot{\gamma} \to \infty$ in the considered Cross-type case. In Section 4.3, results obtained with both the Newtonian (2.41) and Cross-type (2.44) Mori–Tanaka model are compared to results of the FFT-based computational approach presented in Section 2.3.

2.5. Material parameters

In the previous sections 2.2 and 2.4, we discussed some aspects of FFT-based homogenization and analytical modeling of fiber suspensions. In this section, we describe the material and microstructure properties considered in the article. In the following, we are concerned with microstructures of fiber polymer suspensions, and we consider a commercially available polyamide 6 (PA6) [72] as matrix material in all computational studies. A Cross-type material law (2.2) was fitted to PA6 material data available for shear rates $\dot{\gamma}$ in the interval $[1.7, 16300]\,\mathrm{s}^{-1}$ for a temperature of 250°C. The available material data as well as the fit are visualized in Fig. 1, and the resulting model parameters are $\eta_0 = 288.9$ Pa s, $\eta_\infty = 15.0$ Pa s, $k = 10.9 \cdot 10^{-4}$, and $m = 1.1$. For all studied cases with Newtonian matrix behavior, the shear rate dependent matrix viscosity η was chosen as $\eta = \eta_0$.

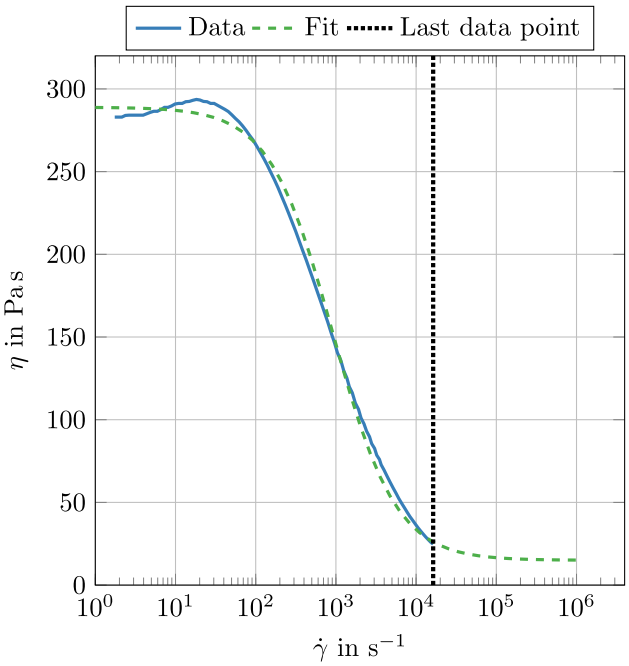

Fig. 1. Material data and Cross-type fit for Ultramid®B3K.

Typical shear rates $\dot{\gamma}$ in compression molding processes are below $5 \cdot 10^1\ \mathrm{s}^{-1}$, while shear rates in injection molding processes are typically kept below $1 \cdot 10^5\ \mathrm{s}^{-1}$ for most materials [73, Sec. 21.6.8], but can go above $1 \cdot 10^6\ \mathrm{s}^{-1}$ in thin-wall and micro molding [74]. To cover some of- the process-relevant shear rate intervals for both compression and injection molding processes, computational investigations were conducted for the macroscopic scalar shear rates

$$\dot{\gamma} \in S_{\dot{\gamma}} = \{a \cdot 10^b\ \mathrm{s}^{-1} |\ a = 1, 2, 5;\ b = 1, 2, 3, 4\} \cup \{10^5\}. \tag{2.45}$$

Because the Cross-type matrix viscosity changes only slightly for shear rates $\dot{\gamma}$ larger than $1 \cdot 10^5\ \mathrm{s}^{-1}$, shear rates above $1 \cdot 10^5\ \mathrm{s}^{-1}$ were not investigated.

Overall, a thorough orientation state dependent investigation of the suspension viscosity takes a large amount of computational resources. Since the focus of this article lies in identifying the underlying effects of shear-thinning rheology on the fiber suspension viscosity, one particular orientation state was considered for our investigations. Because strongly oriented fiber orientation states are very common in injection and compression molding [75,76], the second order fiber orientation tensor $\boldsymbol{N}$ of the considered microstructure was chosen to be transversely isotropic such that

$$\boldsymbol{N} = \begin{bmatrix} 0.8 & 0 & 0 \\ 0 & 0.1 & 0 \\ 0 & 0 & 0.1 \end{bmatrix} \boldsymbol{e}_i \otimes \boldsymbol{e}_j. \tag{2.46}$$

While this particular choice of fiber orientation state is strongly oriented, other fiber orientation states are of research and engineering interest as well. However, to focus on the particularities and influence of the Cross-type matrix material on the non-Newtonian fiber suspension viscosity, we restrict the scope of this article to the given orientation state. The symmetry of the underlying microstructure is also reflected in the suspension viscosity $\bar{\underline{\underline{V}}}$. Hence, if the computational volume element was chosen sufficiently large, we expect the computed suspension viscosity $\bar{\underline{\underline{V}}}$ to be transversely isotropic as well. We use this fact in Section 4 to complement the volume element study detailed in Section 3.3.

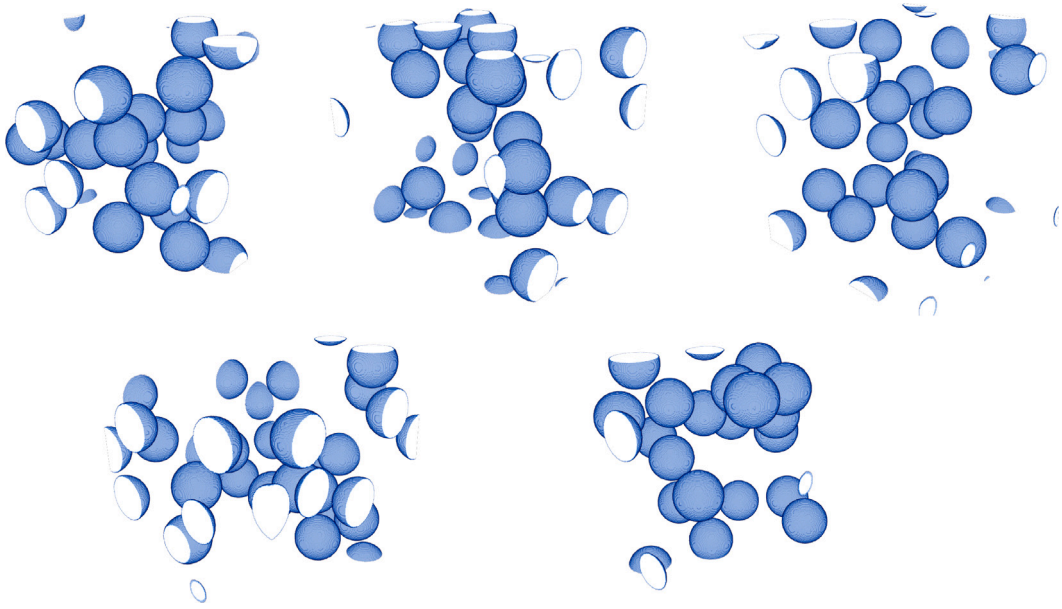

Fig. 2. Five microstructures with a sphere volume fraction of $c_F = 10\%$.

3. Preliminary studies

3.1. Validation against computational results from literature

Traxl et al. [44] investigated the suspension viscosity of rigid spheres suspended in a non-Newtonian matrix fluid using the finite element method. For validation purposes, we compare results obtained with the presented FFT-based homogenization approach to results from Traxl et al. [44]. The microstructures of interest include twenty spheres, contain a sphere volume fraction of $c_S = 10\%$, and were generated based on the mechanical contraction method of Williams–Philipse [77]. The spheres are suspended in a Cross-type (2.2) matrix fluid with the same parameters as in Traxl et al. [44]: $\eta_0 = 1.5$ Pa s, $\eta_\infty = 0.5$ Pa s, $k = 2$, $n = 0.8$. To replicate the procedure detailed in Traxl et al. [44], five different realizations of the microstructure were generated and resolved with 256^3 voxels, see Fig. 2. As effective loads, twenty-one effective stresses $\underline{\bar{\boldsymbol{\tau}}}$ of the form $\underline{\bar{\boldsymbol{\tau}}} = [0,\ 0,\ 0,\ 0,\ 0,\ \bar{\tau}_{12}]$ were applied to each microstructure, with the effective stress components $\bar{\tau}_{12}$ being linearly spaced on the interval $[0.089, 0.914]$ Pa. Here, the interval bounds of the effective stress components $\bar{\tau}_{12}$ were extracted from the results of Traxl et al. [44]. For each microstructure m, the resulting effective shear rate $\dot{\gamma}_m^{\mathrm{FFT}}(\bar{\tau}_{12})$ in response to the loads $\underline{\bar{\boldsymbol{\tau}}}$ was measured, and then used to calculate an average effective shear rate $\dot{\gamma}_{\mathrm{A}}^{\mathrm{FFT}}(\bar{\tau}_{12})$ via

$$\dot{\gamma}_{\mathrm{A}}^{\mathrm{FFT}}(\bar{\tau}_{12}) = \frac{1}{5}\sum_{i=1}^{5} \dot{\gamma}_i^{\mathrm{FFT}}(\bar{\tau}_{12}). \tag{3.1}$$

Subsequently, the average effective shear rate $\dot{\gamma}_{\mathrm{A}}^{\mathrm{FFT}}(\bar{\tau}_{12})$ was compared to the average effective shear rate $\dot{\gamma}_{\mathrm{A}}^{\mathrm{lit}}(\bar{\tau}_{12})$ given in Traxl et al. [44] via the deviation d_{num}, which we define as

$$d_{\mathrm{num}} = \frac{|\dot{\gamma}_{\mathrm{A}}^{\mathrm{lit}}(\bar{\tau}_{12}) - \dot{\gamma}_{\mathrm{A}}^{\mathrm{FFT}}(\bar{\tau}_{12})|}{\dot{\gamma}_{\mathrm{A}}^{\mathrm{lit}}(\bar{\tau}_{12})}. \tag{3.2}$$

The resulting effective shear rate-stress curves for the FFT-based method is in very good agreement with the results from Traxl et al. [44], see Fig. 3(a). This is emphasized by the deviation d_{num}, which lies below 2.3% for all investigated effective loads $\underline{\bar{\boldsymbol{\tau}}}$, see Fig. 3(b).

3.2. Resolution study

The resolution of the microstructure discretization is limited by computational resources, namely memory and runtime. To determine a suitable resolution that accommodates limited resources, and allows for an appropriately small error, we conducted a resolution study for the cases of Newtonian and Cross-type (2.2) matrix behavior. We conducted the study for a fixed fiber aspect ratio $r_a = 10$ and for fiber volume fractions $c_F \in \{5\%, 10\%, 15\%, 20\%, 25\%\}$. Since the inter fiber distance decreases with increasing volume fraction c_F, the effective stress $\bar{\boldsymbol{\tau}}$ of the suspension is expected to be more sensitive to resolution effects for higher fiber volume fractions c_F. Consequently, we chose the maximum considered volume fraction $c_F = 25\%$ for all volume elements in the resolution study. To reduce the amount of necessary voxels, we investigated two types of voxel discretizations, namely binary and composite voxels [78]. For the composite voxels, we used the general dual mixing rule

$$\bar{\boldsymbol{\tau}}_V = c_M \boldsymbol{\tau}_M + (1 - c_M)\boldsymbol{\tau}_F \tag{3.3}$$

where $\bar{\boldsymbol{\tau}}_V$, c_M, $\boldsymbol{\tau}_M$, and $\boldsymbol{\tau}_F$ are the effective stress, the matrix volume fraction, the matrix stress, and the fiber stress inside the composite voxel, respectively. In the special case of rigid fibers, the fiber stress $\boldsymbol{\tau}_F$ is zero. Hence, the general composite voxel mixing rule (3.3) simplifies to

$$\bar{\boldsymbol{\tau}}_V = c_M \boldsymbol{\tau}_M. \tag{3.4}$$

Like in Bertóti et al. [39], we increased the number of voxels per fiber diameter v/d in dyadic steps for the binary voxels, such that $v/d \in \{5, 10, 20, 40\}$, see Fig. 4.

Hence, a single microstructure was discretized with the resolutions $v/d \in \{5, 10, 20, 40\}$ for binary voxels and $v/d \in \{5, 10, 20\}$ for composite voxels, and the effective stress $\bar{\boldsymbol{\tau}}$ was calculated for all considered shear rates and loading directions.

We define the relative error caused by the resolution as

$$e_{\mathrm{res}} = \frac{\|\bar{\boldsymbol{\tau}} - \bar{\boldsymbol{\tau}}_{\mathrm{fine}}\|_2}{\|\bar{\boldsymbol{\tau}}_{\mathrm{fine}}\|_2}, \tag{3.5}$$

where $\bar{\boldsymbol{\tau}}$ is the effective stress for an arbitrary resolution $v/d < 40$ and $\bar{\boldsymbol{\tau}}_{\mathrm{fine}}$ is the binary voxel result for a resolution of $v/d = 40$. Therefore, the effective stress $\bar{\boldsymbol{\tau}}$ for each resolution, voxel type, and load case is compared to the load specific reference stress $\bar{\boldsymbol{\tau}}_{\mathrm{fine}}$. For a particular voxel type and a given resolution v/d, we define the set S_e that collects the resolution errors e_{res} for all investigated load cases as

$$S_e = \left\{ e_{\mathrm{res}}\left(\bar{\boldsymbol{\tau}}^{(i)}(\dot{\gamma}), \bar{\boldsymbol{\tau}}_{\mathrm{fine}}^{(i)}(\dot{\gamma})\right) \mid i = 1,2,3,4,5,6,\ \dot{\gamma} \in S_{\dot{\gamma}} \right\}, \tag{3.6}$$

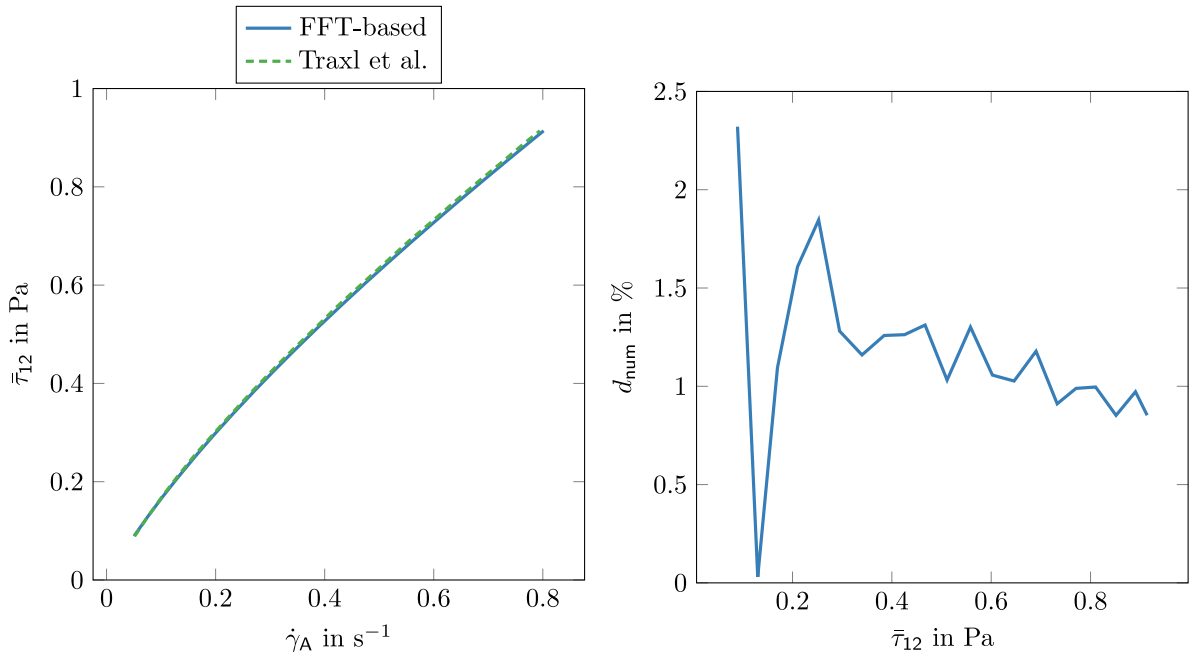

(a) Effective shear rate-stress curves (b) Deviation d_{num}

Fig. 3. Comparison of the effective shear rate-stress curves given in Traxl et al. [44] and the effective shear rate-stress curves obtained from FFT-based simulations, as well as their deviation d_{num} for effective stress components $\bar{\tau}_{12} \in [0.089, 0.914]$ Pa.

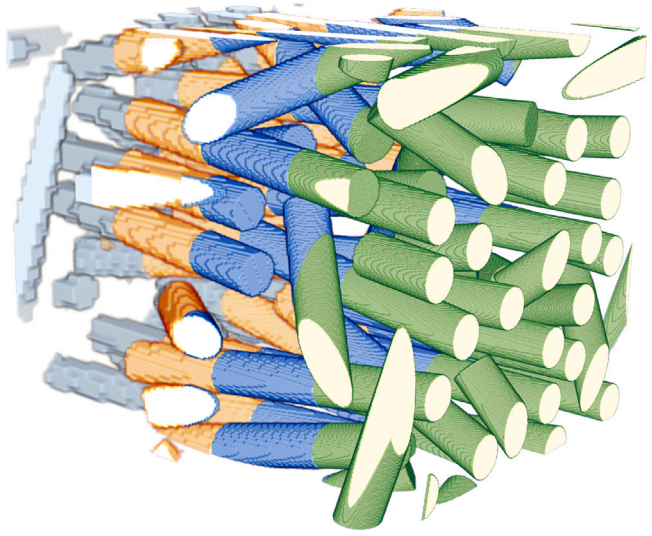

Fig. 4. Microstructure where four differently colored segments are shown with varying voxels per fiber diameter v/d. Segments from left to right: grey ($v/d = 5$), orange ($v/d = 10$), blue ($v/d = 20$), green ($v/d = 40$).

where $\bar{\boldsymbol{\tau}}^{(i)}(\dot{\gamma})$ is the material response to the load case collected in the ith column of $\bar{\underline{\underline{D}}}(\dot{\gamma})$, see Eq. (2.35), and $\bar{\boldsymbol{\tau}}^{(i)}_{\text{fine}}(\dot{\gamma})$ is the corresponding reference stress. Additionally, we define the minimum, maximum, and mean error for a particular voxel type and a particular resolution as

$$e_{\text{min}} = \min S_e, \quad e_{\text{max}} = \max S_e, \quad e_{\text{mean}} = \sum_{e_{\text{res}} \in S_e} e_{\text{res}} / |S_e|, \tag{3.7}$$

where $|S_e|$ denotes the cardinality of the set S_e. The quantitative values for the error measures e_{min}, e_{max}, and e_{mean} are visualized in Fig. 5 for binary and composite voxels and for the resolutions $v/d \in \{5, 10, 20, 40\}$.

For all resolutions, the minimum, maximum and mean errors e_{min}, e_{max}, and e_{mean} decrease with the resolution v/d. In both the Newtonian and Cross-type case, and for all resolutions v/d, the values of the three errors (3.7) are lower for the composite voxels than for the binary voxels. Most notably, the maximum error e_{max} falls below 5% at a resolution $v/d = 20$ for the binary voxel model, but already does so at a resolution $v/d = 10$ when using composite voxels.

Intriguingly, the minimum errors e_{min} are consistently lower in the Cross-type case than in the Newtonian case, while the maximum errors e_{max} remain on a similar level. We note that the lowest errors e_{min} occur, independent of the resolution v/d, for the pure shear load case $\bar{\underline{D}} = \dot{\gamma}[0\ 0\ 0\ 0\ 1\ 0]$ at a shear rate $\dot{\gamma} = 2 \cdot 10^3\ s^{-1}$. The maximum errors e_{max} occur at the lowest investigated shear rate of $\dot{\gamma} = 10\ s^{-1}$ for the elongational load cases which are collected in the 1st, 2nd, and 3rd column of $\bar{\underline{\underline{D}}}$, see Eq. (2.35). Thus, some of the investigated load cases lead to a reduced resolution requirement or the reference solution is less accurate, which is an effect also observed in elastoplastic material models in solid mechanics [79]. To ensure a resolution error e_{res} below 5% for all load cases, a resolution of $v/d = 15$ was chosen for all following computations.

3.3. Volume element size

Like the resolution of the microstructure discretization, the size of the volume element under investigation is limited by computational resources. Appropriate volume element sizes for fiber suspensions with Newtonian matrix behavior with aspect ratios $r_a = 10$ and fiber volume fractions c_F up to 25% were investigated by Bertóti et al. [39]. Depending on the fiber orientation, different representative volume element sizes were identified by Bertóti et al. [39], and in the case of aligned fibers, a volume element of the form $2.2\ell \times 20d \times 20d$ was identified as sufficiently representative. Adding to these insights, we conducted a study to determine a suitable size of the volume element for the considered transversely isotropic orientation state in the Cross-type case, with a fiber aspect ratio $r_a = 10$, and fiber volume fractions $c_F \in \{5\%, 10\%, 15\%, 20\%, 25\%\}$. Because the necessary volume element size grows with the fiber volume fraction c_F, we chose $c_F = 25\%$ for the volume element study. We investigated volume elements of the form $L \times W \times W$, where $L \in \{1.1\ell, 2.2\ell, 3.2\ell\}$ and $W \in \{5d, 10d, 20d\}$

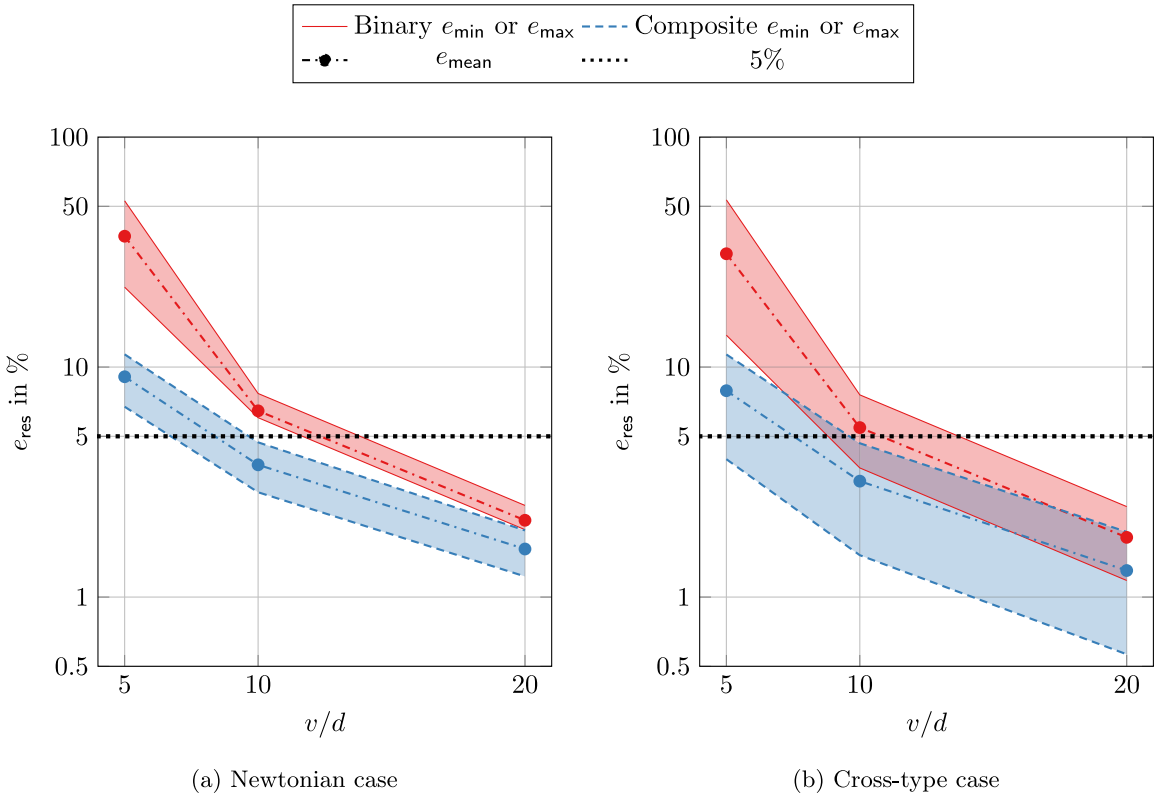

Fig. 5. Convergence of the relative resolution error (3.5) for the Newtonian case (a) and the Cross-type case (b).

Table 1
Mean, standard deviation, and maximum value of the relative error e_{VE} (3.8) in %, computed with ten realizations per combination of length L and width W.

L	W	Mean ± std	Max	L	W	Mean ± std	Max	L	W	Mean ± std	Max
1.2ℓ	5d	37.48 ± 19.0	106.21	2.2ℓ	5d	29.76 ± 15.68	78.97	3.2ℓ	5d	9.71 ± 5.52	27.73
	10d	5.06 ± 4.03	23.89		10d	3.75 ± 2.5	11.11		10d	3.28 ± 1.68	8.55
	20d	3.62 ± 2.28	10.96		20d	1.75 ± 0.82	4.06		20d	1.14 ± 0.51	3.05

with fiber length ℓ and the fiber diameter d, see Fig. 6. To discretize the microstructures, we employed composite voxels and used a resolution of $v/d = 15$, as identified in the previous section.

For every combination of length L and width W, ten different microstructures were generated, and their effective stresses $\bar{\boldsymbol{\tau}}$ were calculated for all considered shear rates (2.45) and loading directions (2.35). We define the relative error caused by the volume element size as

$$e_{\text{VE}} = \frac{\|\bar{\boldsymbol{\tau}} - \bar{\boldsymbol{\tau}}_{\text{ref}}\|_2}{\|\bar{\boldsymbol{\tau}}_{\text{ref}}\|_2}. \tag{3.8}$$

For each individual load case, the effective stress $\bar{\boldsymbol{\tau}}$ of the ten largest microstructures with length $L = 3.2\ell$ and width $W = 20d$ was averaged and chosen as the reference stress $\bar{\boldsymbol{\tau}}_{\text{ref}}$. Thus, for each volume element size, the effective stress $\bar{\boldsymbol{\tau}}$ of each of the ten realizations is compared to the average reference stress $\bar{\boldsymbol{\tau}}_{\text{ref}}$. This allows us to calculate the means and standard deviations of the relative error e_{VE} for each combination of length L and width W, which are collected in Table 1.

First, we note that the mean and standard deviation of the relative error e_{VE} decrease faster with the width W than with the length L. The largest decrease in the mean and standard deviation of e_{VE} occurred when the width W was increased from $W = 5$ to $W = 10$. Thus, an appropriate choice of the volume width is essential to obtain robust results. Overall, we observe that the maximum value of the error e_{VE} falls below the engineering bound of 5% for the sizes $L = 2.2\ell$, $W = 20d$ and $L = 3.2\ell$, $W = 20d$, where the maximum of the error e_{VE} is 4.06% and 3.05%, respectively. With mean errors of 1.75% and 1.14%, and error standard deviations of 0.82% and 0.51%, both sizes $L = 2.2\ell$, $W = 20d$ and $L = 3.2\ell$, $W = 20d$ show similar error characteristics. Consequently, we consider the size of the volume element $L = 2.2\ell$, $W = 20d$ as sufficient, which aligns with the results for aligned fibers in the Newtonian case of Bertóti et al. [39]. Accordingly, we choose $L = 2.2\ell$, $W = 20d$ for all further investigations.

4. Computational investigations

4.1. Spatial representation of the suspension viscosity through a scalar elongational viscosity

Böhlke and Brüggemann [80] introduced a simple method to visualize an anisotropic stiffness tensor. We modify this approach to calculate the fiber polymer suspension's resistance to elongational flow in a particular direction via an elongational viscosity η_{app}. In the general non-Newtonian case, we define a direction-dependent, elongational viscosity η_{app}

$$\eta_{\text{app}}(\dot{\gamma}, c_{\text{F}}, \boldsymbol{d}) = \underline{a}(\boldsymbol{d})^{\mathsf{T}}\, \underline{\underline{\bar{V}}}(\dot{\gamma}, c_{\text{F}})\, \underline{a}(\boldsymbol{d}) \;\approx\; \mathbb{V}(\dot{\gamma}, c_{\text{F}}) \cdot (\boldsymbol{d} \otimes \boldsymbol{d} \otimes \boldsymbol{d} \otimes \boldsymbol{d}), \tag{4.1}$$

where $\underline{a}(\boldsymbol{d})$ denotes the components of $\boldsymbol{d}\otimes\boldsymbol{d}$ in Mandel notation, $\boldsymbol{d}$ is the elongation direction, and the suspension viscosity $\underline{\underline{\bar{V}}}(\dot{\gamma}, c_{\text{F}})$ is calculated via Eq. (2.33) as an approximation of the true suspension viscosity tensor $\mathbb{V}(\dot{\gamma}, c_{\text{F}})$. Since the true suspension viscosity tensor $\mathbb{V}$ has the minor and major symmetries, it is defined by 21 components. As a consequence, the suspension viscosity $\underline{\underline{\bar{V}}}(\dot{\gamma}, c_{\text{F}})$ can be completely described

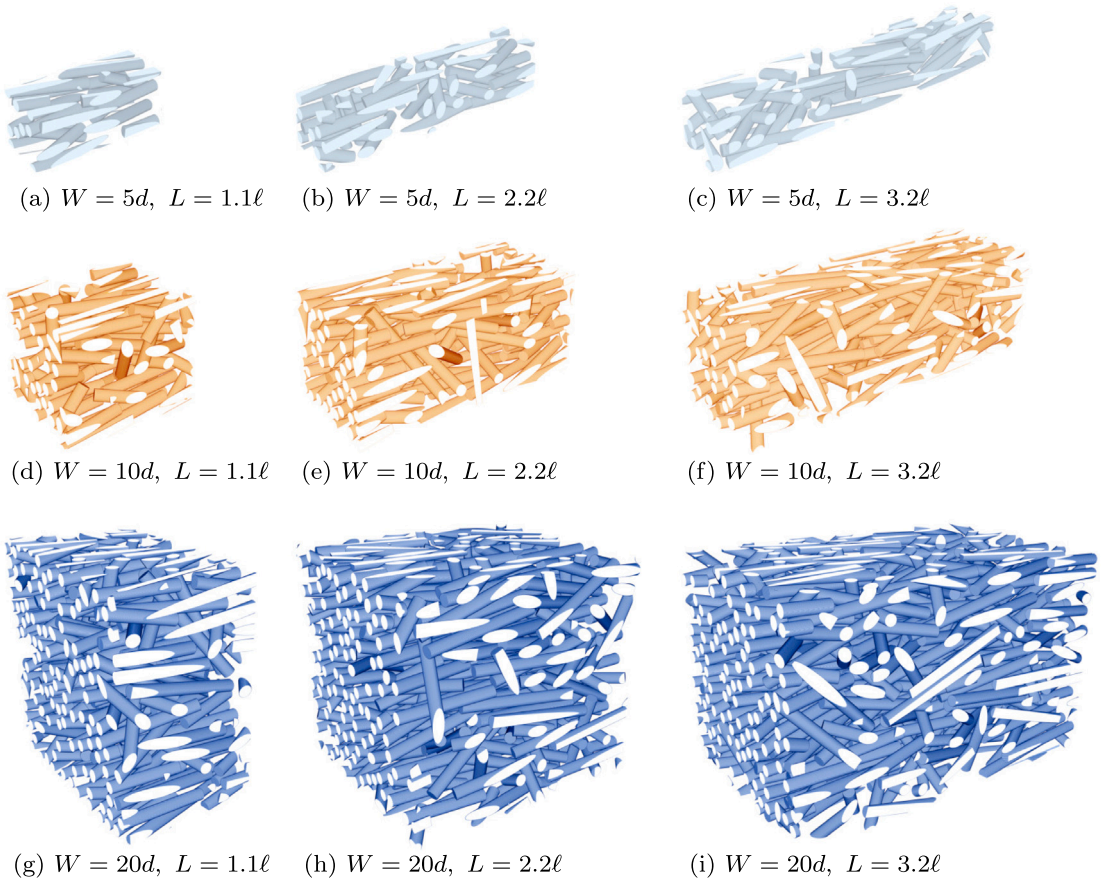

(a) $W = 5d,\ L = 1.1\ell$ (b) $W = 5d,\ L = 2.2\ell$ (c) $W = 5d,\ L = 3.2\ell$

(d) $W = 10d,\ L = 1.1\ell$ (e) $W = 10d,\ L = 2.2\ell$ (f) $W = 10d,\ L = 3.2\ell$

(g) $W = 20d,\ L = 1.1\ell$ (h) $W = 20d,\ L = 2.2\ell$ (i) $W = 20d,\ L = 3.2\ell$

Fig. 6. Comparison of microstructures with dimensions $L \times W \times W$, lengths $L \in \{1.1\ell, 2.2\ell, 3.2\ell\}$, and widths $W \in \{5d, 10d, 20d\}$.

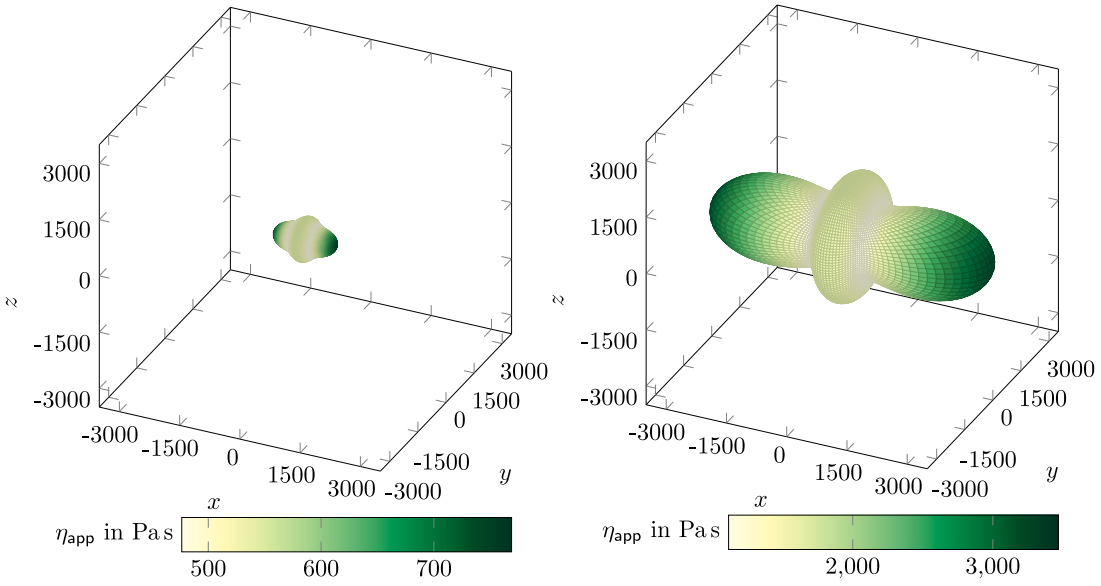

(a) $c_F = 5\%$ (b) $c_F = 25\%$

Fig. 7. Apparent viscosity η_{app} in the Newtonian case for fiber volume fractions $c_F = 5\%$ (a) and $c_F = 25\%$ (b).

by a scalar elongational viscosity and a scalar dilatational viscosity, see He and Curnier [81, Sec. 4.3]. The elongational and dilatational viscosity then contain the information of 15 and 6 components of the suspension viscosity $\underline{\underline{\bar{V}}}(\dot{\gamma}, c_F)$, respectively.

However, due to incompressibility, all information contained in the suspension viscosity $\underline{\underline{\bar{V}}}(\dot{\gamma}, c_F)$ is completely and uniquely encoded via the elongational viscosity $\eta_{app}(\dot{\gamma}, c_F, \boldsymbol{d})$ [81, Sec. 4.3]. This holds in both the Newtonian and Cross-type case. Thus, in the following, we use the

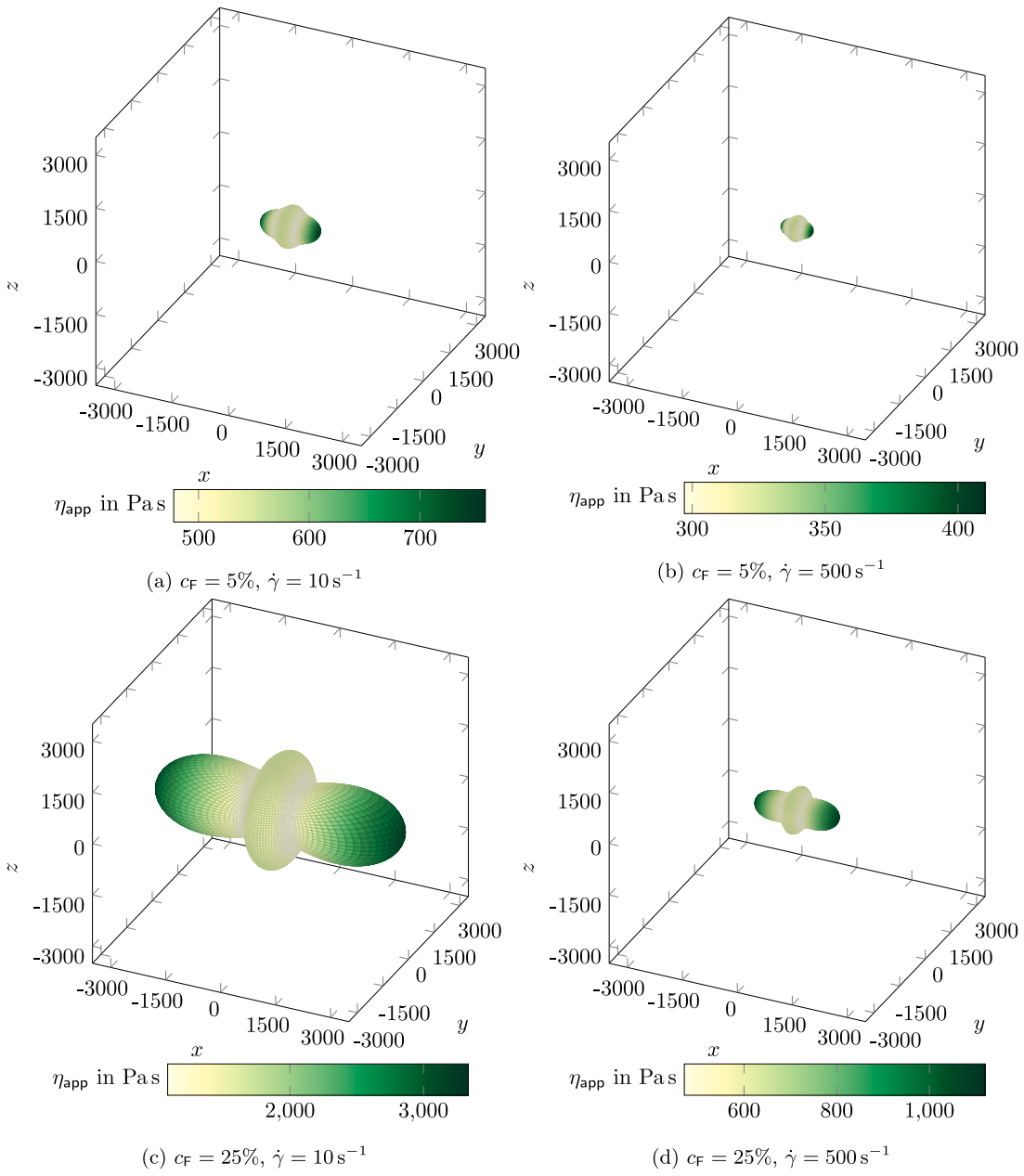

Fig. 8. Apparent viscosity η_{app} in the Cross-type case for combinations of fiber volume fractions c_F and shear rate $\dot{\gamma}$: $c_F = 5\%, \dot{\gamma} = 10\,s^{-1}$ (a), $c_F = 5\%, \dot{\gamma} = 500\,s^{-1}$ (b), $c_F = 25\%, \dot{\gamma} = 10\,s^{-1}$ (c), and $c_F = 25\%, \dot{\gamma} = 500\,s^{-1}$ (d).

elongational viscosity $\eta_{app}(\dot{\gamma}, c_F)$ as a tool to completely visualize and qualitatively understand the suspension viscosity $\underline{\underline{\bar{V}}}(\dot{\gamma}, c_F)$. For the special case of an isotropic suspension viscosity, and a uniaxial elongation direction $\boldsymbol{d}$, the elongational viscosity $\eta_{app}(\dot{\gamma}, \boldsymbol{d})$ is related to the shear viscosity $\eta(\dot{\gamma})$ (2.2) such that $\eta_{app}(\dot{\gamma}, \boldsymbol{d}) = 4\eta(\dot{\gamma})/3$. In the Newtonian case, the viscosity tensor components $\underline{\underline{\bar{V}}}(\dot{\gamma}, c_F)$ are independent of the shear rate $\dot{\gamma}$. The dependence of the elongational viscosity $\eta_{app}(\dot{\gamma}, c_F, \boldsymbol{d})$ and the suspension viscosity $\underline{\underline{\bar{V}}}(\dot{\gamma}, c_F)$ on the shear rate $\dot{\gamma}$, fiber volume fraction c_F, and elongation direction $\boldsymbol{d}$ will be omitted for notational clarity. Note that the colormap limits in Figs. 7 and 8 are chosen to highlight the respective extrema of the elongational viscosity η_{app}, and that differences in magnitude are visualized by the size of the viscosity bodies.

In Figs. 7 and 8, we observe that for both the Newtonian and Cross-type case, the elongational viscosity η_{app} is large when the direction $\boldsymbol{d}$ is aligned with the principal fiber orientation axis. This is expected, since flow resistance along the cylindrical fibers is higher than in other flow directions. Furthermore, the elongational viscosity η_{app} for both cases increases with growing fiber volume fraction c_F in all directions $\boldsymbol{d}$. However, in the Cross-type case, the elongational viscosity η_{app} decreases with the shear rate $\dot{\gamma}$ in all directions $\boldsymbol{d}$. Depending on the value of the shear rate $\dot{\gamma}$, one effect outweighs the other.

Note that the minimum value of the elongational viscosity η_{app} does not occur perpendicular to the principal fiber orientation axis x in both cases, because of incompressibility.

4.2. Polar representation and material anisotropy

While spatial representations of the elongational viscosity η_{app} provide intuition and qualitative understanding of the underlying viscosity matrix $\underline{\underline{\bar{V}}}$, cuts through the viscosity bodies shown in the previous section allow for a more focused discussion of the occurring effects. As noted in the previous section, the fiber volume fraction c_F has a strong influence on the suspension viscosity $\underline{\underline{\bar{V}}}$. Because the matrix $\underline{\underline{\bar{V}}}$ should

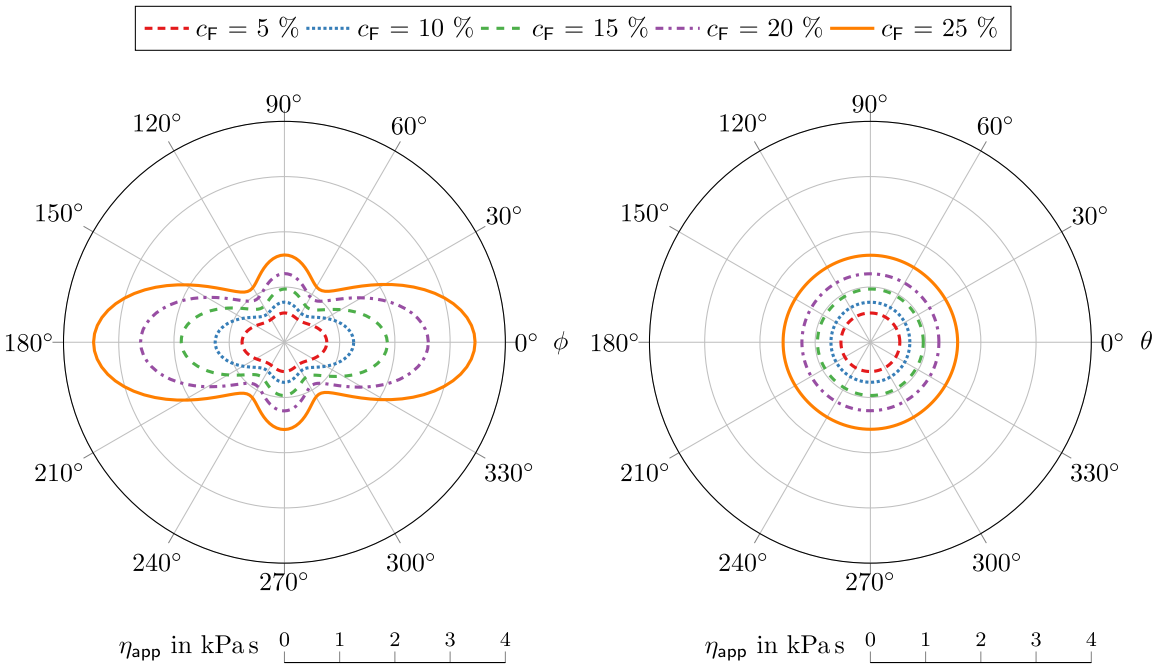

(a) η_{app} in the x-y plane (b) η_{app} y-z plane

Fig. 9. Apparent viscosity η_{app} in the $x-y$ and $y-z$ plane, for fiber volume fractions $c_F \in \{5, 10, 15, 20, 25\}\%$ in the Newtonian case.

Table 2
Apparent viscosities η^y_{app} and η^x_{app} in the Newtonian case for fiber volume fractions $c_F \in \{5, 10, 15, 20, 25\}\%$.

c_F in %	5	10	15	20	25
η^y_{app} in Pa s	530	726	964	1 243	1 581
η^x_{app} in Pa s	769	1 258	1 872	2 615	3 468

be transversely isotropic, see Section 2.5, we will discuss the effect of the fiber volume fraction c_F and the shear rate $\dot{\gamma}$ on the suspension viscosity $\underline{\underline{\bar{V}}}$ by focusing on the elongational viscosities η^x_{app} and η^y_{app} in x and y direction.

In Section 4.1 we noted that the elongational viscosity η_{app} increases with the fiber volume fraction c_F in all directions $\boldsymbol{d}$. Additionally, as shown in Figs. 9 and 10, the changes of the elongational viscosities η^y_{app} and η^x_{app} with the fiber volume fraction c_F increase with the fiber volume fraction c_F itself. In the Newtonian case, the viscosity η^y_{app} increases from 530 Pa s to 1 581 Pa s as the fiber volume fraction c_F changes from 5% to 25%, see Table 2. In contrast, the elongational viscosity η^x_{app} increases from 769 Pa s to 3 468 Pa s as the fiber volume fraction c_F increases from 5% to 25%. Thus, the elongational viscosities η^y_{app} and η^x_{app} increase by 198% and 351%, respectively.

In the Cross-type case, the elongational viscosity η_{app} depends on the shear rate $\dot{\gamma}$, as highlighted by Fig. 10 and Table 3. At a fiber volume fraction $c_F = 5\%$, the elongational viscosity η^y_{app} decreases from 529 Pa s to 30 Pa s as the shear rate $\dot{\gamma}$ changes from $10\,s^{-1}$ to $10^5\,s^{-1}$. In contrast, the elongational viscosity η^x_{app} decreases from 759 Pa s to 43 Pa s as the shear rate $\dot{\gamma}$ changes from $10\,s^{-1}$ to $10^5\,s^{-1}$. Hence, both elongational viscosities η^y_{app} and η^x_{app} decrease by the same factor of around 94%. However, for a lower shear rate $\dot{\gamma} = 10^3$ Pa s, the elongational viscosities η^y_{app} and η^x_{app} decrease differently by the factors 57% and 62%, respectively. We observe a similar change for the higher fiber volume fraction $c_F = 25\%$. In this case, the elongational viscosities η^y_{app} and η^x_{app} also decrease by around 94% as the shear rate $\dot{\gamma}$ changes from $10\,s^{-1}$ to $10^5\,s^{-1}$. Again, for a lower shear rate $\dot{\gamma} = 10^3$ Pa s, the elongational viscosities η^y_{app} and η^x_{app} decrease differently by the factors 75% and 78%, respectively. As a result, we conclude that for shear rates $\dot{\gamma}$ where the matrix behavior is non-Newtonian the elongational viscosities η^x_{app} and η^y_{app} vary stronger with the shear rate for higher fiber volume fraction c_F. Also, since the elongational viscosities η^y_{app} and η^x_{app} change by different factors in both the Newtonian and Cross-type case for a shear rate $\dot{\gamma} = 10^3\,s^{-1}$, the material anisotropy changes with varying fiber volume fraction c_F and shear rate $\dot{\gamma}$, see Fig. 11. We discuss these changes in the following.

For the transversely isotropic symmetry of the suspension viscosity $\underline{\underline{\bar{V}}}$, its anisotropy is characterized by the elongational viscosities η^x_{app} and η^y_{app}. For further investigation we also use a third elongational viscosity η^z_{app} in z direction. Each parameter represents the value of the elongational viscosity η_{app} for an elongation direction $\boldsymbol{d}$ in x-, y-, and z-direction, respectively. Thus, the fractions

$$f_1 = \frac{\eta^x_{app}}{\eta^y_{app}}, \quad \text{and} \quad f_2 = \frac{\eta^x_{app}}{\eta^z_{app}} \tag{4.2}$$

serve as a measure of directional anisotropy. For a theoretical, perfectly transversely isotropic suspension viscosity, both fractions f_1 and f_2 assume the same value. As described in Section 2.5, we prescribed a transversely isotropic, second order orientation tensor (2.46) for all considered microstructures. Hence, we also expect a transversely isotropic suspension viscosity $\underline{\underline{\bar{V}}}$ if the volume element size for the computational investigations was chosen sufficiently large.

To test if the volume element size was chosen appropriately, we define the relative deviation

$$e_{dev} = \frac{|f_1 - f_2|}{|f_1|}, \tag{4.3}$$

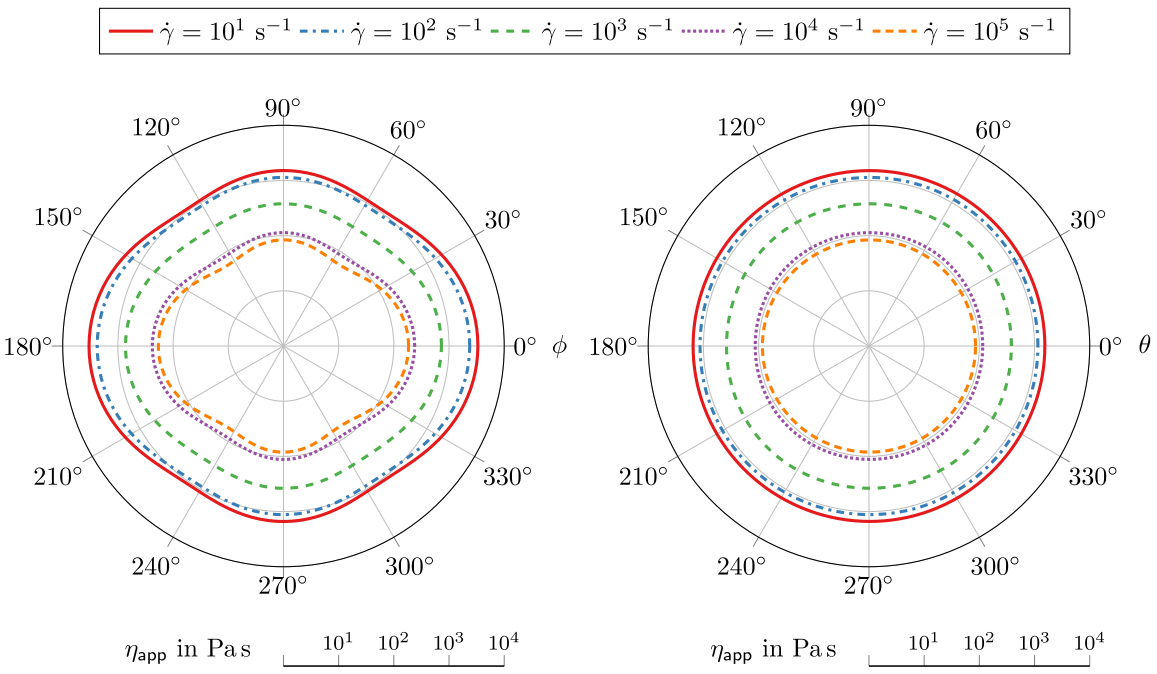

(a) η_{app} in the x-y plane (b) η_{app} in the y-z plane

Fig. 10. $x-y$ and $y-z$ plane cuts of the Cross-type, elongational viscosity bodies for fiber volume fractions $c_{\mathrm{F}} = 25\%$ and shear rates $\dot{\gamma} \in \{10^1, 10^2, 10^3, 10^4, 10^5\}\,\mathrm{s}^{-1}$.

Table 3
Apparent viscosities η^y_{app} and η^x_{app} in the Cross-type case for fiber volume fractions $c_{\mathrm{F}} \in \{5, 10, 15, 20, 25\}\%$ and shear rates $\dot{\gamma} \in \{10, 10^3, 10^5\}\,\mathrm{s}^{-1}$.

c_{F} in %	5			15			25		
$\dot{\gamma}$ in s^{-1}	10^1	10^3	10^5	10^1	10^3	10^5	10^1	10^3	10^5
η^y_{app} in Pa s	529	226	30	939	295	52	1 515	379	84
η^x_{app} in Pa s	759	287	43	1 818	494	101	3 336	729	185

and evaluate the relative deviation e_{dev} for both the Newtonian and Cross-type case. For all considered shear rates $\dot{\gamma}$ and volume fractions c_{F}, the deviation e_{dev} is smaller than 2% in both the Newtonian and the Cross-type case. Therefore, the values of the fractions f_1 and f_2 differ only slightly from each other, and the expected symmetry of the material is captured with an error that is sufficiently small for engineering purposes. The elongational viscosity η_{app} in the y-z plane, as shown in Figs. 9(b) and 10(b), illustrate the material symmetry further, since the polar plots of the elongational viscosity η_{app} are circular for all fiber volume fractions c_{F} and shear rates $\dot{\gamma}$. Since we consider the volume elements as representative, we will discuss the dependence of both fractions f_1 and f_2 on the fiber volume fraction c_{F} and the shear rate $\dot{\gamma}$ as shown in Fig. 11.

In the Newtonian case, both fractions f_1 and f_2 grow significantly from 1.45 at a volume fraction $c_{\mathrm{F}} = 5\%$ to 2.19 at a volume fraction $c_{\mathrm{F}} = 25\%$. Because the matrix behavior in the Cross-type case is approximately Newtonian for low shear rates $\dot{\gamma}$, the values of the fractions f_1 and f_2 in the Cross-type case for a shear rate $\dot{\gamma} = 10\,\mathrm{s}^{-1}$ are similar to those in the Newtonian case. As the shear rate $\dot{\gamma}$ grows, the values of the fractions f_1 and f_2 decrease up to a shear rate $\dot{\gamma}_{\mathrm{min}} \approx 10^3\,\mathrm{s}^{-1}$, where they reach their respective minima. Because more fibers are likely to be packed close to each other for higher volume fractions c_{F}, higher velocity gradients occur at lower macroscopic shear rates $\dot{\gamma}$. This, in turn, decreases the local matrix viscosity. Consequently, the minimum of the fractions f_1 and f_2 occurs at lower shear rates as the fiber volume fraction grows. For a fiber volume fraction $c_{\mathrm{F}} = 25\%$, the minimum of the fractions f_1 and f_2 is attained at a shear rate $\dot{\gamma} = 10^3\,\mathrm{s}^{-1}$, whereas, for a fiber volume fraction $c_{\mathrm{F}} = 5\%$, the minimum is attained at a shear rate $\dot{\gamma} = 2 \cdot 10^3\,\mathrm{s}^{-1}$.

Also, the maximum absolute changes

$$\Delta f(c_{\mathrm{F}}) = f(c_{\mathrm{F}}, 10\,\mathrm{s}^{-1}) - f(c_{\mathrm{F}}, \dot{\gamma}_{\mathrm{min}}) \tag{4.4}$$

increase with the fiber volume fraction c_{F}, e.g., $\Delta f(c_{\mathrm{F}}) = 17\%$ and $\Delta f(c_{\mathrm{F}}) = 28\%$ for fiber volume fractions c_{F} of 5% and 25%, respectively. In contrast, the maximum relative changes

$$\Delta f(c_{\mathrm{F}}) = \frac{f(c_{\mathrm{F}}, 10\,\mathrm{s}^{-1}) - f(c_{\mathrm{F}}, \dot{\gamma}_{\mathrm{min}})}{f(c_{\mathrm{F}}, 10\,\mathrm{s}^{-1})} \tag{4.5}$$

lie between 12% to 14% for all investigated fiber volume fractions.

4.3. Comparison to mean-field results

In the following, we compare the computational results with mean-field estimates. In the Newtonian and Cross-type cases, we use the Mori–Tanaka model (2.41) to calculate the apparent mean-field viscosity $\eta^{\mathrm{MF}}_{\mathrm{app}}$. Then, we compare the apparent mean-field viscosity $\eta^{\mathrm{MF}}_{\mathrm{app}}$ with the apparent computational viscosity $\eta^{\mathrm{FFT}}_{\mathrm{app}}$ via the deviation

$$e_{\mathrm{MF}} = \frac{\left|\eta^{\mathrm{MF}}_{\mathrm{app}} - \eta^{\mathrm{FFT}}_{\mathrm{app}}\right|}{\eta^{\mathrm{FFT}}_{\mathrm{app}}}. \tag{4.6}$$

To reduce dimensional complexity, and to avoid compromising the comparison with potential interpolation errors, as discussed in Section 4.1, we focus our discussion on the two scalar quantities η^x_{app} and η^y_{app}. The results for the Newtonian and the Cross-type case are shown in Figs. 12 and 13, as well as Fig. 14.

In the Newtonian case, the elongational viscosities η^x_{app} and η^y_{app} obtained via the mean-field method are lower than the ones obtained

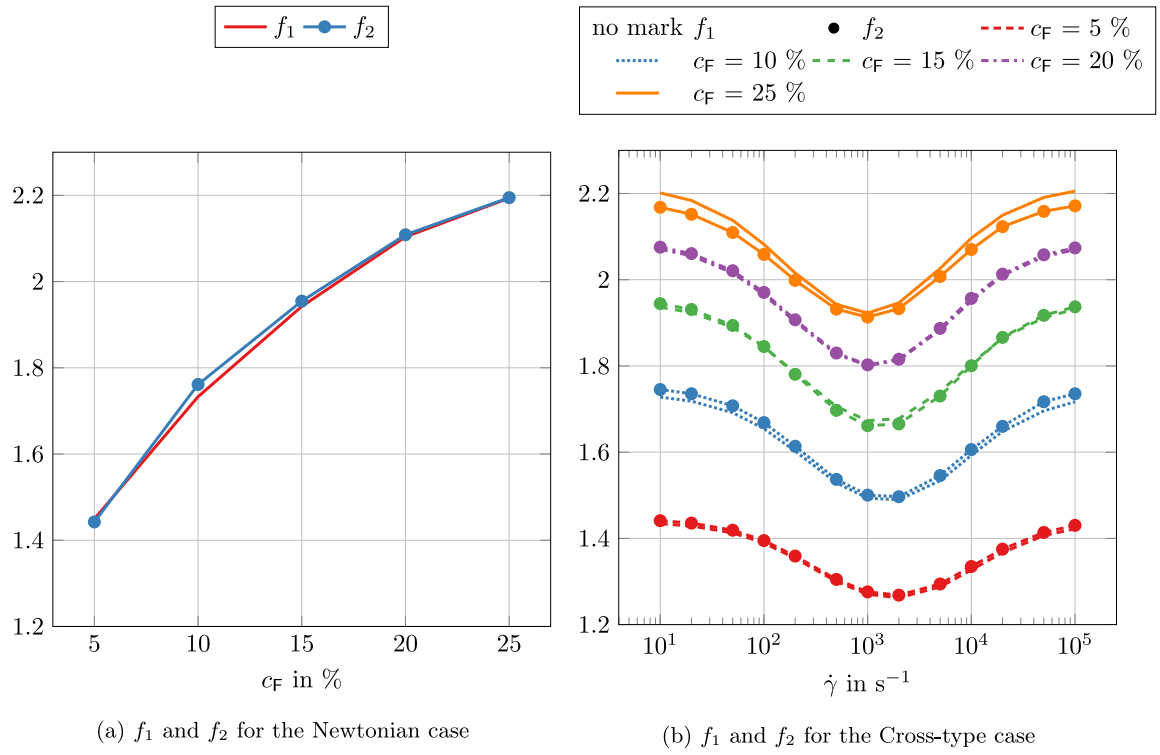

(a) f_1 and f_2 for the Newtonian case

(b) f_1 and f_2 for the Cross-type case

Fig. 11. Anisotropy fractions f_1 and f_2 (4.2) for the Newtonian and the Cross-type case, $c_F \in \{5, 10, 15, 20, 25\}\%$, $\dot{\gamma} \in [10, 10^5]\,s^{-1}$.

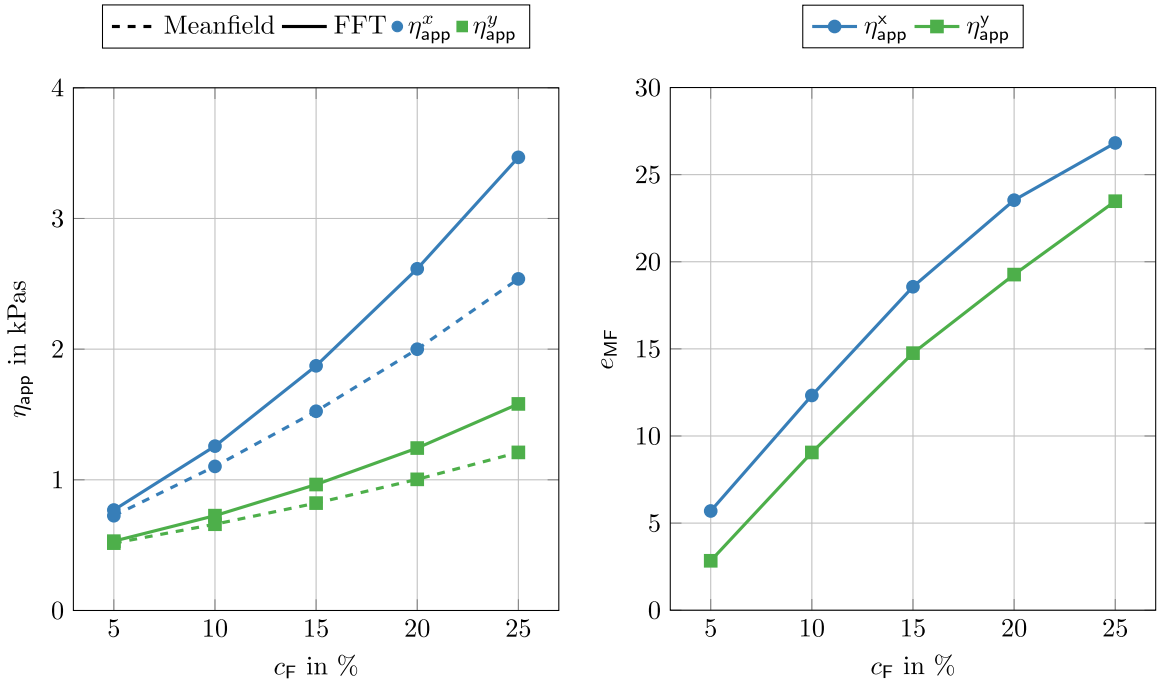

(a) Apparent viscosities η^x_{app} and η^y_{app}

(b) Deviation e_{MF}

Fig. 12. Apparent viscosities η^x_{app} and η^y_{app} for the mean-field model and the FFT-based computational method, and deviation e_{MF} (4.3) for fiber volume fractions $c_F \in \{5, 10, 15, 20, 25\}\%$ in the Newtonian case.

via the FFT-based computational method. Also, for a fiber volume fraction $c_F = 5\%$, the mean-field and FFT-based results for η^x_{app} and η^y_{app} can still be considered similar for engineering purposes, as the deviation e_{MF} is below 5.7%. However, for increasing fiber volume fractions c_F, the deviation e_{MF} increases monotonically up to 26.8% for the elongational viscosity η^x_{app} and 23.5% for the elongational viscosity η^y_{app}.

In the Cross-type case, for shear rates $\dot{\gamma} \approx 10\,s^{-1}, \dot{\gamma} \approx 10^5\,s^{-1}$, we observe the same results for the deviation e_{MF} as in the Newtonian case. This is a direct result of the two Newtonian regions of the Cross-type matrix viscosity η at the shear rate limits $\dot{\gamma} \to 0\,s^{-1}$ and $\dot{\gamma} \to \infty\,s^{-1}$. The largest deviation e_{MF} occurs for a shear rate $\dot{\gamma} = 10^3\,s^{-1}$, where the matrix nonlinearity is highest. As we already observed for the

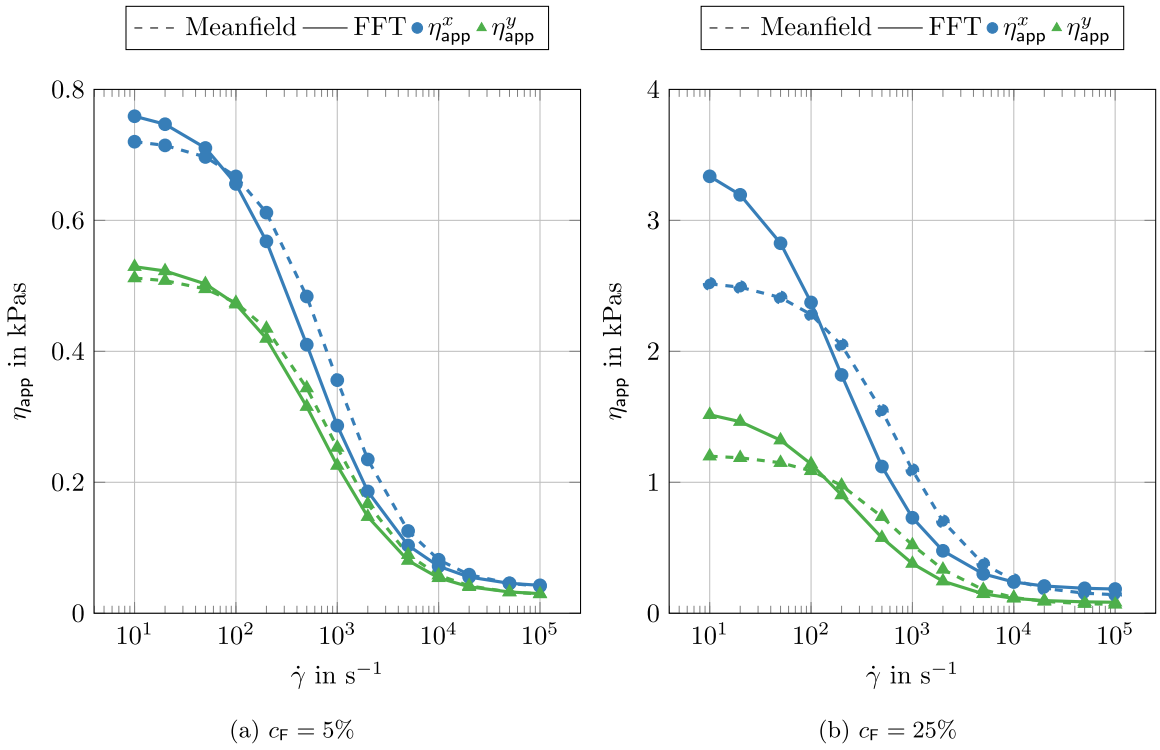

Fig. 13. Apparent viscosities η^x_{app} and η^y_{app} for the mean-field model and the FFT-based computational method for fiber volume fractions $c_{\text{F}} \in \{5, 25\}\%$ and shear rates $\dot{\gamma} \in [10, 10^5]\,\text{s}^{-1}$ in the Cross-type case.

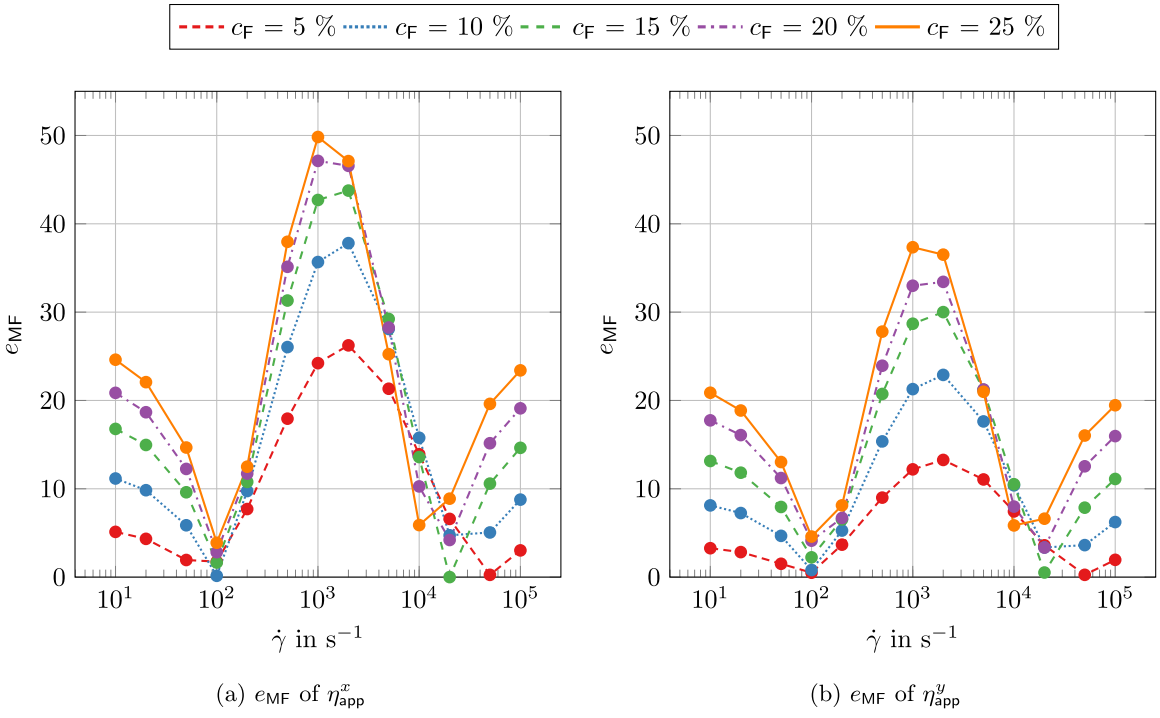

Fig. 14. Deviation e_{MF} (4.3) of the elongational viscosities η^x_{app} and η^y_{app} for fiber volume fractions $c_{\text{F}} \in \{5, 10, 15, 20, 25\}\%$ and shear rates $\dot{\gamma} \in [10, 10^5]\,\text{s}^{-1}$ in the Cross-type case.

anisotropy measures f_1 and f_2 in Section 4.1, the fiber volume fraction c_{F} influences the shear rate $\dot{\gamma}$ at which the maximum deviation e_{MF} occurs. In particular, for both elongational viscosities η^x_{app} and η^y_{app}, the maximum observed deviation for a fiber volume fraction $c_{\text{F}} = 25\%$ occurs at a lower shear rate $\dot{\gamma} = 10^3\,\text{s}^{-1}$, whereas it occurs at a shear rate $\dot{\gamma} = 2 \cdot 10^3\,\text{s}^{-1}$ for a fiber volume fraction $c_{\text{F}} = 5\%$. As an additional consequence of the Cross-type material law (2.2), the curves of the elongational viscosities η^x_{app} and η^y_{app} for the two calculation methods intersect twice. For the fiber volume fractions $c_{\text{F}} = 5\%$ and $c_{\text{F}} = 25\%$, the first intersection occurs at shear rates $\dot{\gamma} \approx 10^2\,\text{s}^{-1}$ while the second intersection occurs in the shear rate interval $[10^4, 5 \cdot 10^4]\,\text{s}^{-1}$, depending on the fiber volume fraction c_{F}. For higher fiber volume fractions c_{F} the

second intersection occurs at lower macroscopic shear rates $\dot{\gamma}$, because the decreased fiber to fiber distance leads to higher microscopic shear rates. Consequently we observe an earlier transition into the second Newtonian regime at the shear rate limit $\dot{\gamma} \to \infty\,\mathrm{s}^{-1}$. In between the intersections of the elongational viscosity curves, the elongational viscosity η_{app} obtained via the mean-field model is higher than for the computational approach.

5. Conclusion

This work was devoted to study the effect of shear-thinning matrix behavior on the effective viscosity of fiber suspensions. We focused our considerations on shear rates of interest for engineering manufacturing processes, like injection and compression molding. For our investigations, we made use of a Cross-type viscosity model and an FFT-based computational method to determine the effective viscosity of fiber suspensions over a wide range of shear rates. We found the resolution error of the microstructure discretization to be dependent on the shear rate and load direction, with the minimum resolution error occurring at medium shear rates and pure shear loads. To our surprise, we found the representative volume element size to be highly similar in a Newtonian case with aligned microstructure and a Cross-type case with transversely isotropic microstructure. Over the considered shear rate interval, we found the Cross-type suspension viscosity to vary strongly in magnitude and in degree of anisotropy. Finally, we observed substantial deviations between the computational estimates and Mori–Tanaka type mean-field estimates for the suspension viscosity.

In subsequent work, the presented Cross-type FFT-based homogenization procedure could improve prediction capabilities of engineering process simulations by providing enhanced estimates for the suspension viscosity. Also, combined with an efficient upscaling technique such as Deep Material Networks [82–85], the Cross-type FFT-based procedure could be employed on an element level in nonlinear, component scale process simulations. Furthermore, the Cross-type FFT-based procedure could be used in the validation, improvement and development of mean-field models for the viscosity of nonlinear suspensions. As the first article to investigate the effective viscosity of non-Newtonian fiber suspensions in the context of FFT-based computational homogenization, the scope of this article was restricted to fibers of aspect ratio ten, a selected transversely isotropic fiber orientation state, and Cross-type shear-thinning rheology. From a physical perspective, effects like shear-thickening rheology, temperature dependence, and polymer crystallization might also be incorporated into the computational procedure to increase versatility. Furthermore, investigations of suspensions with higher fiber aspect ratios and different fiber orientation states are of engineering interest as well, and could be elements of future research.

Declaration of competing interest

The authors declare that they have no known competing financial interests or personal relationships that could have appeared to influence the work reported in this paper.

Data availability

Data will be made available on request.

Acknowledgments

The research documented in this manuscript has been funded by the Deutsche Forschungsgemeinschaft (DFG, German Research Foundation), Germany, project number 255730231, within the International Research Training Group “Integrated engineering of continuous-discontinuous long fiber reinforced polymer structures“ (GRK 2078/2). The support by the German Research Foundation (DFG) is gratefully acknowledged. We thank the anonymous reviewers for their helpful comments.

Author contributions

The present study was conceptualized by B. Sterr, D. Wicht, M. Schneider, and T. Böhlke. B. Sterr, D. Wicht, and M. Schneider implemented and validated the software. B. Sterr performed the simulations, analyzed and visualized the data, and drafted the manuscript. The original manuscript draft was extensively reviewed and edited by B. Sterr, A. Hrymak, M. Schneider, and T. Böhlke. Resources were provided by M. Schneider and T. Böhlke. The research project was supervised by A. Hrymak, M. Schneider and T. Böhlke.

References

[1] P. Kennedy, R. Zheng, Flow Analysis of Injection Molds, Carl Hanser Verlag GmbH Co KG, Munich, Germany, 2013.
[2] V. Goodship, ARBURG Practical Guide to Injection Moulding, Smithers Rapra, Shawbury, United Kingdom, 2017.
[3] J. Castro, G. Tomlinson, Predicting molding forces in SMC compression molding, Polym. Eng. Sci. 30 (24) (1990) 1568–1573.
[4] T. Karl, D. Gatti, T. Böhlke, B. Frohnapfel, Coupled simulation of flow-induced viscous and elastic anisotropy of short-fiber reinforced composites, Acta Mech. 232 (6) (2021) 2249–2268.
[5] D. Binding, Capillary and contraction flow of long-(glass) fibre filled polypropylene, Composites Manuf. 2 (3–4) (1991) 243–252.
[6] A. Poslinski, M. Ryan, R. Gupta, S. Seshadri, F. Frechette, Rheological behavior of filled polymeric systems i. yield stress and shear-thinning effects, J. Rheol. 32 (7) (1988) 703–735.
[7] J.M. Krishnan, A.P. Deshpande, P.S. Kumar, Rheology of Complex Fluids, Springer, Berlin, Heidelberg, Germany, 2010.
[8] W. Sutherland, A dynamical theory of diffusion for non-electrolytes and the molecular mass of albumin, Lond. Edinb. Dublin Philos. Mag. J. Sci. 9 (54) (1905) 781–785.
[9] A. Einstein, Eine neue Bestimmung der Moleküldimensionen (Ph.D. thesis), ETH Zurich, 1905.
[10] G. Batchelor, The stress system in a suspension of force-free particles, J. Fluid Mech. 41 (3) (1970) 545–570.
[11] G. Batchelor, The stress generated in a non-dilute suspension of elongated particles by pure straining motion, J. Fluid Mech. 46 (4) (1971) 813–829.
[12] S.M. Dinh, R.C. Armstrong, A rheological equation of state for semiconcentrated fiber suspensions, J. Rheol. 28 (3) (1984) 207–227.
[13] E.S. Shaqfeh, G.H. Fredrickson, The hydrodynamic stress in a suspension of rods, Phys. Fluids A 2 (1) (1990) 7–24.
[14] T. Karl, T. Böhlke, Unified mean-field modeling of viscous short-fiber suspensions and solid short-fiber reinforced composites, Arch. Appl. Mech. 92 (12) (2022) 3695–3727.
[15] C.J. Petrie, The rheology of fibre suspensions, J. Non-Newton. Fluid Mech. 87 (2–3) (1999) 369–402.
[16] L. Leal, The slow motion of slender rod-like particles in a second-order fluid, J. Fluid Mech. 69 (2) (1975) 305–337.
[17] P. Kaloni, V. Stastna, Steady-shear rheological behavior of the suspension of spherical particles in a second-order fluid, Polym. Eng. Sci. 23 (8) (1983) 465–470.
[18] P. Brunn, The slow motion of a rigid particle in a second-order fluid, J. Fluid Mech. 82 (3) (1977) 529–547.
[19] P. Brunn, The motion of rigid particles in viscoelastic fluids, J. Non-Newton. Fluid Mech. 7 (4) (1980) 271–288.
[20] J.D. Goddard, Tensile stress contribution of flow-oriented slender particles in Non-Newtonian fluids, 1976.
[21] J. Goddard, The stress field of slender particles oriented by a Non-Newtonian extensional flow, J. Fluid Mech. 78 (1) (1976) 177–206.
[22] J. Goddard, Tensile behavior of power-law fluids containing oriented slender fibers, J. Rheol. 22 (6) (1978) 615–622.
[23] C. Mobuchon, P.J. Carreau, M.-C. Heuzey, M. Sepehr, G. Ausias, Shear and extensional properties of short glass fiber reinforced polypropylene, Polym. Compos. 26 (3) (2005) 247–264.
[24] R.B. Pipes, J. Hearle, A. Beaussart, A. Sastry, R. Okine, A constitutive relation for the viscous flow of an oriented fiber assembly, J. Compos. Mater. 25 (9) (1991) 1204–1217.
[25] R.B. Pipes, D.W. Coffin, S.F. Shuler, P. Šimáček, Non-newtonian constitutive relationships for hyperconcentrated fiber suspensions, J. Compos. Mater. 28 (4) (1994) 343–351.
[26] B. Souloumiac, M. Vincent, Steady shear viscosity of short fibre suspensions in thermoplastics, Rheol. Acta 37 (3) (1998) 289–298.
[27] J. Férec, E. Bertevas, B.C. Khoo, G. Ausias, N. Phan-Thien, The effect of shear-thinning behaviour on rod orientation in filled fluids, J. Fluid Mech. 798 (2016) 350–370.
[28] H.-C. Tseng, A constitutive equation for fiber suspensions in viscoelastic media, Phys. Fluids 33 (7) (2021) 071702.

[29] J. Férec, E. Bertevas, B.C. Khoo, G. Ausias, N. Phan-Thien, A rheological constitutive model for semiconcentrated rod suspensions in Bingham fluids, Phys. Fluids 29 (7) (2017) 073103.

[30] A.J. Favaloro, H.-C. Tseng, R.B. Pipes, A new anisotropic viscous constitutive model for composites molding simulation, Composites A 115 (2018) 112–122.

[31] O. Marin, K. Gustavsson, A.-K. Tornberg, A highly accurate boundary treatment for confined Stokes flow, Comput. & Fluids 66 (2012) 215–230.

[32] F. Balboa Usabiaga, B. Kallemov, B. Delmotte, A. Bhalla, B. Griffith, A. Donev, Hydrodynamics of suspensions of passive and active rigid particles: a rigid multiblob approach, Commun. Appl. Math. Comput. Sci. 11 (2) (2017) 217–296.

[33] H. Moulinec, P. Suquet, A fast numerical method for computing the linear and nonlinear mechanical properties of composites, C. R. Acad. Sci., Paris II (1994).

[34] H. Moulinec, P. Suquet, A numerical method for computing the overall response of nonlinear composites with complex microstructure, Comput. Methods Appl. Mech. Engrg. 157 (1–2) (1998) 69–94.

[35] T. Kanit, S. Forest, I. Galliet, V. Mounoury, D. Jeulin, Determination of the size of the representative volume element for random composites: statistical and numerical approach, Int. J. Solids Struct. 40 (13–14) (2003) 3647–3679.

[36] F. Willot, Fourier-based schemes for computing the mechanical response of composites with accurate local fields, C. R. Mec. 343 (3) (2015) 232–245.

[37] S. Mezhoud, V. Monchiet, M. Bornert, D. Grande, Computation of macroscopic permeability of doubly porous media with fft based numerical homogenization method, Eur. J. Mech. B Fluids 83 (2020) 141–155.

[38] F. Tu, J. Tong, M. Wang, Z. Chen, S. Qi, An FFT-based Galerkin method for the effective permeability of porous material, Internat. J. Numer. Methods Engrg. (2022).

[39] R. Bertóti, D. Wicht, A. Hrymak, M. Schneider, T. Böhlke, A computational investigation of the effective viscosity of short-fiber reinforced thermoplastics by an FFT-based method, Eur. J. Mech. B Fluids 90 (2021) 99–113.

[40] J. Segurado, R.A. Lebensohn, J. LLorca, Computational homogenization of polycrystals, Adv. Appl. Mech. 51 (2018) 1–114.

[41] M. Schneider, A review of nonlinear FFT-based computational homogenization methods, Acta Mech. 232 (6) (2021) 2051–2100.

[42] Sergio Lucarini, Manas V Upadhyay, Javier Segurado, FFT based approaches in micromechanics: fundamentals, methods and applications, Modelling and Simulation in Materials Science and Engineering 30 (2) (2021) 023002.

[43] J. Domurath, M. Saphiannikova, J. Férec, G. Ausias, G. Heinrich, Stress and strain amplification in a dilute suspension of spherical particles based on a bird–carreau model, J. Non-Newton. Fluid Mech. 221 (2015) 95–102.

[44] R. Traxl, C. Pichler, R. Lackner, Micromechanics-based assessment of the effective viscosity of suspensions of generalized-newtonian fluids embedding noncolloidal angular/spheroidal pores and particles, J. Rheol. 64 (4) (2020) 899–913.

[45] O. Švec, J. Skoček, H. Stang, M.R. Geiker, N. Roussel, Free surface flow of a suspension of rigid particles in a non-newtonian fluid: A lattice Boltzmann approach, J. Non-Newton. Fluid Mech. 179 (2012) 32–42.

[46] M.M. Cross, Rheology of Non-Newtonian fluids: a new flow equation for pseudoplastic systems, J. Colloid Sci. 20 (5) (1965) 417–437.

[47] M.M. Cross, Kinetic interpretation of Non-Newtonian flow, J. Colloid Interface Sci. 33 (1) (1970) 30–35.

[48] J. Ericksen, Anisotropic fluids, Arch. Ration. Mech. Anal. 4 (1) (1959) 231–237.

[49] J. Ericksen, Transversely isotropic fluids, Kolloid-Z. 173 (2) (1960) 117–122.

[50] M. Silhavy, The Mechanics and Thermodynamics of Continuous Media, Springer Science & Business Media, Berlin, Heidelberg, Germany, 2013.

[51] P. Suquet, Local and Global Aspects in the Mathematical Theory of Plasticity, in: A. Sawczuk, G. Bianchi (Eds.), Plasticity Today, Elsevier Appl. Sc. Pub., London, 1985, pp. 279–310.

[52] P. Suquet, Elements of homogenization for inelastic solid mechanics, in: Homogenization Techniques for Composite Media, 1987.

[53] A. Chambolle, T. Pock, An introduction to continuous optimization for imaging, Acta Numer. 25 (2016) 161–319.

[54] T. Böhlke, A. Bertram, The reuss bound of the strain rate potential of viscoplastic FCC polycrystals, Tech. Mech.-Eur. J. Eng. Mech. 23 (2–4) (2003) 184–194.

[55] T. Böhlke, The voigt bound of the stress potential of isotropic viscoplastic fcc polycrystals, Arch. Mech. 56 (6) (2004) 425–445.

[56] M. Kabel, S. Fliegener, M. Schneider, Mixed boundary conditions for FFT-based homogenization at finite strains, Comput. Mech. 57 (2) (2016) 193–210.

[57] D. Wicht, M. Schneider, T. Böhlke, An efficient solution scheme for small-strain crystal-elasto-viscoplasticity in a dual framework, Comput. Methods Appl. Mech. Engrg. 358 (2020) 112611.

[58] L. Armijo, Minimization of functions having lipschitz continuous first partial derivatives, Pacific J. Math. 16 (1) (1966) 1–3.

[59] A.A. Goldstein, On steepest descent, J. Soc. Ind. Appl. Math. Ser A Control 3 (1) (1965) 147–151.

[60] M. Schneider, The sequential addition and migration method to generate representative volume elements for the homogenization of short fiber reinforced plastics, Comput. Mech. 59 (2) (2017) 247–263.

[61] F.H. Harlow, J.E. Welch, Numerical calculation of time-dependent viscous incompressible flow of fluid with free surface, Phys. Fluids 8 (12) (1965) 2182–2189.

[62] J. Barzilai, J.M. Borwein, Two-point step size gradient methods, IMA J. Numer. Anal. 8 (1) (1988) 141–148.

[63] R.S. Dembo, S.C. Eisenstat, T. Steihaug, Inexact Newton methods, SIAM J. Numer. Anal. 19 (2) (1982) 400–408.

[64] M. Schneider, A dynamical view of nonlinear conjugate gradient methods with applications to FFT-based computational micromechanics, Comput. Mech. 66 (1) (2020) 239–257.

[65] M. Schneider, Lippmann–Schwinger solvers for the computational homogenization of materials with pores, Internat. J. Numer. Methods Engrg. 121 (22) (2020) 5017–5041.

[66] M. Schneider, On the effective viscosity of a periodic suspension–analysis of primal and dual formulations for Newtonian and Non-Newtonian solvents, Math. Methods Appl. Sci. 39 (12) (2016) 3309–3327.

[67] S.G. Advani, C.L. Tucker III, The use of tensors to describe and predict fiber orientation in short fiber composites, J. Rheol. 31 (8) (1987) 751–784.

[68] K. Kanatani, Distribution of directional data and fabric tensors, Internat. J. Engrg. Sci. 22 (2) (1984) 149–164.

[69] R. Bertóti, Modeling the Flow-Induced Anisotropic Effective Viscosity of Fiber Suspensions by Mean-Field and Full-Field Homogenization (Doctoral thesis), Karlsruher Institut für Technologie (KIT), 2021.

[70] J.R. Willis, Bounds and self-consistent estimates for the overall properties of anisotropic composites, J. Mech. Phys. Solids 25 (3) (1977) 185–202.

[71] R. Bertóti, T. Böhlke, Flow-induced anisotropic viscosity in short FRPs, Mech. Adv. Mater. Mod. Process. 3 (1) (2017) 1–12.

[72] Ultramid®B3K polyamide 6 material data, 2020, https://www.campusplastics.com/campus/de/datasheet/Ultramid%C2%AE+B3K/BASF/20/3a22f000. (Accessed 26 September 2020).

[73] J.R.L. Valero, Plastics injection molding: scientific molding, recommendations, and best practices, Carl Hanser Verlag GmbH Co KG, Munich, Germany, 2020.

[74] W. Friesenbichler, I. Duretek, J. Rajganesh, S.R. Kumar, Measuring the pressure dependent viscosity at high shear rates using a new rheological injection mould, Polimery 56 (1) (2011) 58–62.

[75] M. Vincent, T. Giroud, A. Clarke, C. Eberhardt, Description and modeling of fiber orientation in injection molding of fiber reinforced thermoplastics, Polymer 46 (17) (2005) 6719–6725.

[76] C. Park, W. Lee, Y. Yoo, E. Kim, A study on fiber orientation in the compression molding of fiber reinforced polymer composite material, J. Mater Process. Technol. 111 (1–3) (2001) 233–239.

[77] S. Williams, A. Philipse, Random packings of spheres and spherocylinders simulated by mechanical contraction, Phys. Rev. E 67 (5) (2003) 051301.

[78] M. Kabel, A. Fink, M. Schneider, The composite voxel technique for inelastic problems, Comput. Methods Appl. Mech. Engrg. 322 (2017) 396–418.

[79] M. Schneider, D. Wicht, Superconvergence of the effective cauchy stress in computational homogenization of inelastic materials, International Journal for Numerical Methods in Engineering 124 (4) (2023) 959–978.

[80] T. Böhlke, C. Brüggemann, Graphical representation of the generalized Hooke's law, Tech. Mech. 21 (2) (2001) 145–158.

[81] Q.-C. He, A. Curnier, A more fundamental approach to damaged elastic stress–strain relations, Int. J. Solids Struct. 32 (10) (1995) 1433–1457.

[82] Z. Liu, C. Wu, M. Koishi, A deep material network for multiscale topology learning and accelerated nonlinear modeling of heterogeneous materials, Comput. Methods Appl. Mech. Engrg. 345 (2019) 1138–1168.

[83] S. Gajek, M. Schneider, T. Böhlke, On the micromechanics of deep material networks, J. Mech. Phys. Solids 142 (2020) 103984.

[84] S. Gajek, M. Schneider, T. Böhlke, An FE-DMN method for the multiscale analysis of thermomechanical composites, Comput. Mech. 69 (5) (2022) 1087–1113.

[85] A.P. Dey, F. Welschinger, M. Schneider, S. Gajek, T. Böhlke, Training deep material networks to reproduce creep loading of short fiber-reinforced thermoplastics with an inelastically-informed strategy, Arch. Appl. Mech. 92 (9) (2022) 2733–2755.